10/
A 16-96950 ①

SANDIA REPORT

SAND96-8219 • UC ~~1409~~ 104
Unlimited Release
Printed February 1996

Coal Combustion Science
Quarterly Progress Report
October - December 1994

Principal Investigators: Larry L. Baxter
Kevin A. Davis
Robert H. Hurt
Nancy Y.C. Yang

MASTER

Edited by Donald R. Hardesty

This report has been reproduced from the best available copy.

Available to DOE and DOE contractors from:

Office of Scientific and Technical Information
P. O. Box 62
Oak Ridge, TN 37831

Prices available from (615) 576-8401, FTS 626-8401

Available to the public from:

National Technical Information Service
U.S. Department of Commerce
5285 Port Royal Rd.
Springfield, VA 22161

COAL COMBUSTION SCIENCE

QUARTERLY PROGRESS REPORT

OCTOBER — DECEMBER 1994

Submitted By: Donald R. Hardesty
Sandia National Laboratories, Livermore
Combustion Research Facility

Submitted To: Philip Goldberg
Pittsburgh Energy Technology Center

3/4

DISCLAIMER

Portions of this document may be illegible in electronic image products. Images are produced from the best available original document.

COAL COMBUSTION SCIENCE
QUARTERLY PROGRESS REPORT — OCTOBER - DECEMBER 1994

Donald R. Hardesty
Combustion Research Facility
Sandia National Laboratories
Livermore, California   94551-0969

This document is a quarterly status report of the Coal Combustion Science Project that is being conducted at the Combustion Research Facility, Sandia National Laboratories, Livermore, California. The information reported is for the period October - December 1994.

The objective of this work is to support the Office of Fossil Energy in executing research on coal combustion science. This project consists of basic research on coal combustion that supports both the Pittsburgh Energy Technology Center (PETC) Direct Utilization Advanced Research and Technology Development Program, and the International Energy Agency (IEA) Coal Combustion Science Project.

Specific tasks include:

Task 1:   Kinetics and Mechanisms of Pulverized Coal Char Combustion

The objective of this task is to characterize the combustion behavior of selected U.S. coals under conditions relevant to industrial pulverized coal-fired furnaces. Work is being done in four areas: (a) kinetics of heterogeneous fuel particle populations; (b) char combustion kinetics at high carbon conversion; (c) the role of particle structure and the char formation process in combustion and; (d) unification of the Sandia char combustion data base. This data base on the high temperature reactivities of chars from strategic U.S. coals will permit identification of important fuel-specific trends and development of predictive capabilities for advanced coal combustion systems.

The principal investigator on this task is Robert H. Hurt.

Task 2:   Deposit Growth and Property Development in Coal-Fired Furnaces

The objectives of this task are to provide a self-consistent database of simultaneously measured, time-resolved, ash deposit properties in well-controlled and well-defined environments and to provide analytical expressions that relate deposit composition and structure to deposit properties of immediate relevance to PETC's Combustion 2000 program. The task includes the development and use of diagnostics to monitor, *in situ* and in real time, deposit properties, including information on both the structure and composition of the deposits.

The principal investigator on this task is Larry L. Baxter.

TABLE OF CONTENTS

COAL COMBUSTION SCIENCE

QUARTERLY PROGRESS REPORT
OCTOBER — DECEMBER 1994

EXECUTIVE SUMMARY

Task 1: The Kinetics and Mechanisms of Pulverized Coal Char Combustion

Work this quarter focused on Subtasks 1.2 and 1.3. Under Subtask 1.2, our investigation of combustion-induced char carbon crystalline transformations was extended to two additional coals (Beulah lignite, PSOC 1507D, and Pittsburgh #8, PSOC 1451D) to understand the effect of rank. This work includes continued use of High Resolution Transmission Electron Microscopy (HRTEM) to examine the microstructure of the unburned coal and char particles. HRTEM has now been applied at Sandia to two biomass chars , one lignite, two high volatile bituminous coals, one low-volatile bituminous coal and two residual carbon samples from commercial boilers. The present report describes the new results in detail and presents an overview of the effect of rank on carbon crystalline transformations under entrained flow combustion conditions.

Also under Subtask 1.2, time-resolved carbon conversions were determined for a series of chars from four coals undergoing combustion in the CCL hot-walled reactor. High conversions (up to 99% on a char basis) were achieved in a single pass, allowing the final burnout region to be examined without capture and reinjection techniques. The measured conversions are currently being compared to the predictions of the global kinetic models proposed previously [Hurt and Mitchell, 1992] with emphasis on the high conversion region. Discrepancies between data and prediction in the high burnout region will be used to test the advanced char oxidation model under development. This work will be presented in detail in the next quarterly report.

Under Subtask 1.3, initial captive particle image sequences were obtained for selected density fractions of two coals prepared in the laboratory of Professor Jack Crelling at Southern Illinois University (SIU). This work is part of the collaborative effort with SIU and Imperial College on coal heterogeneity and its implications for carbon burnout prediction. The initial experiments were designed to understand the qualitative combustion mechanisms for coal particles of differing density and petrographic composition. The initial data provide information on: (1) swelling, (2) ash/carbon interactions, (3) physical transformations in the late stages of combustion (such as fragmentation and microscale densification), and (4) statistical variations in single particle burnout times. Particularly interesting are the images revealing nonuniform swelling in the inertinite-rich heavy fraction of the Middleburg coal. These results are being reviewed by the project team (Gibbins and Crelling) and will be reported in detail next quarter.

Task 2: Deposit Growth and Property Development in Coal-Fired Furnaces

During this quarter, Tunable diode laser (TDL) spectra of alkali vapors (NaCl) were obtained. We believe the technique used to obtain these spectra can be extended to obtain *in situ*, quantitative

concentration measurements for a variety of alkali-containing vapors. The work during this quarter demonstrated an ability to obtain spectra under conditions involving beam steering and strong temperature gradients. Future work will address the issues of particle interference. Individual lines in the NaCl spectrum were resolved and, late in the quarter, the bandhead was detected.

In addition, during the quarter, Fourier transform infrared (FTIR) emission spectroscopy was used to monitor differences in iron oxidation states in a comparitive investigation of deposits generated under low-NO_x burner conditions and those generated under traditional burner configurations. Clear differences in the spectra were observed and these differences are consistent with the known optical properties of iron-containing slags and deposits.

Also this quarter, an algorithm for predicting the reflectance and emittance properties of particulate layers was completed. This accounts for dependent and independent scattering, particle size, porosity, chemical composition, and angles of incidence, observation, and inclination. The technique has yet to be validated by comparison to measured spectra, although the latter have been collected.

Future Work

On the char combustion task, during the next quarter, analysis of the high conversion data from the hot-walled reactor experiments will be completed, presented and compared to global model predictions. Progress will also be made next quarter on the formulation and testing of a char deactivation submodel. Additional captured particle imaging (CPI) experiments are planned on the density fractions supplied by the laboratory of Professor John Crelling at SIU. Progress will also be made on the long-overdue upgrade of the CCL computer and electronics systems.

On the ash deposition task, during the next quarter, development of the tunable diode laser diagnostic system will continue. Alternate beam modulation techniques will be tested and further attempts to locate the NaCl bandhead will be pursued. Also, a sealed, high-temperature gas cell will be designed to allow reference spectra to be obtained. Analyses of the first phase of the emission FTIR spectroscopy analyses of SiC surfaces in combustion environments will be completed. The theoretical description of the emissivity of particulate layers will also be expanded.

PROJECT TITLE:	**COAL COMBUSTION SCIENCE**
	TASK 1: KINETICS AND MECHANISMS OF PULVERIZED COAL CHAR COMBUSTION
ORGANIZATION:	**Sandia National Laboratories, California**
CONTRACT:	**FWP 0709**
REPORTING PERIOD:	**October 1 - December 31, 1994**
REPORTED BY:	**R. H. Hurt, N.Y.C. Yang, K. A. Davis, and D. R. Hardesty**
	Phone: (510) 294-2321

OBJECTIVE FOR TASK 1

The objective of Task 1 is to characterize the combustion behavior of selected U.S. coals under conditions relevant to industrial pulverized coal-fired furnaces. In Sandia's Coal Combustion Laboratory (CCL), optical techniques are used to obtain high-resolution images of individual burning coal char particles and to measure, *in situ*, their temperatures, sizes, and velocities. Detailed models of combustion transport processes are then used to determine kinetic parameters describing the combustion behavior as a function of coal type and combustion environment. Partially reacted char particles are also sampled and characterized with advanced materials diagnostics to understand the critical physical and chemical transformations that influence reaction rates and burnout times. The ultimate goal of the task is the establishment of a data base of the high temperature reactivities of chars from strategic U.S. coals, from which important trends may be identified and predictive capabilities developed.

During FY95, research consists of three subtasks described below. The work is a continuation of activities begun under the FY92 - FY94 project plan. A fourth subtask, *Unification of the Sandia Char Combustion Data Base*, was completed during FY94.

SUBTASK 1.1 KINETICS OF HETEROGENEOUS FUEL PARTICLE POPULATIONS

The objective of this subtask is to develop quantitative descriptions of single-particle combustion behavior and to identify their implications for global rates and for the performance of combustion systems. Experiments in the CCL provide a wealth of unique information on the combustion behavior of single particles as distinguished from macroscopic samples. Kinetic expressions based on population statistics are being developed that more accurately describe the char combustion process as it proceeds into the important region of high carbon conversion. One-dimensional combustion models are being applied to char particle populations, exhibiting realistic heterogeneity in size and reactivity, to identify the important mechanisms leading to unburned carbon in fly ash.

SUBTASK 1.2   CHAR COMBUSTION KINETICS TO HIGH CARBON CONVERSION

The amount of unburned carbon in fly ash is an important concern in the design and operation of pulverized coal fired boilers. High carbon content represents a loss of efficiency, and prevents the sale of the fly ash byproduct as a raw material for the cement or construction industries. The objective of this subtask is to determine char oxidation kinetics valid to high carbon conversion (> 99%) and to identify and understand the mechanisms determining unburned carbon levels in fly ash from pulverized coal combustion. Fly ash samples are generated under carefully controlled laboratory conditions, and the mode of occurrence and properties of the residual carbon will be characterized. The high-temperature combustion reactivity of the residual carbon is measured and carbon transformations occurring during the combustion process are characterized. The ultimate goal of the subtask is the development and validation of an advanced char oxidation model for accurate prediction of residual carbon levels. This requires integration of the coal-rank-dependent reactivity model with a model for char-burnout-dependent combustion kinetics.

SUBTASK 1.3   THE ROLE OF PARTICLE STRUCTURE AND THE CHAR FORMATION PROCESS IN COMBUSTION

In pulverized coal combustion the process of devolatilization determines, to a large extent, the properties and thus the reactivity of the resulting char. Swelling coals, in particular, produce a variety of char particle morphologies ranging from dense consolidated particles to thin or thick walled cenospheres, depending in part on devolatilization conditions. The objective of this subtask is to generalize the kinetic results obtained in the CCL to other devolatilization and combustion environments, through an improved understanding of the char formation process and its relationship to char combustion rates and burnout times. This is being achieved through a combination of flow reactor experiments and high-resolution, single-particle imaging.

During FY95, work is continuing on these three subtasks. We anticipate completion of Subtask 1.1 during the second quarter of FY95, Subtask 1.3 by the end of FY95, and completion of Subtask 1.2 in FY96.

SUMMARY OF TECHNICAL PROGRESS DURING THIS QUARTER

Work this quarter focused on Subtasks 1.2 and 1.3. Under Subtask 1.2, our investigation of combustion-induced char carbon crystalline transformations was extended to two additional coals (Beulah lignite, PSOC 1507D, and Pittsburgh #8, PSOC 1451D) to understand the effect of rank. This work includes continued use of High Resolution Transmission Electron Microscopy (HRTEM) to examine the microstructure of the unburned coal and char particles. HRTEM has now been applied at Sandia to two biomass chars , one lignite, two high volatile bituminous coals, one low-volatile bituminous coal and two residual carbon samples from commercial boilers. The present report describes the new results in detail and presents an overview of the effect of rank on carbon crystalline transformations under entrained flow combustion conditions.

Also under Subtask 1.2, time-resolved carbon conversions were determined for a series of chars from four coals undergoing combustion in the CCL hot-walled reactor. High conversions (up to 99% on a char basis) were achieved in a single pass, allowing the final burnout region to be

examined without capture and reinjection techniques. The measured conversions are currently being compared to the predictions of the global kinetic models proposed previously [Hurt and Mitchell, 1992] with emphasis on the high conversion region. Discrepancies between data and prediction in the high burnout region will be used to test the advanced char oxidation model under development. This work will be presented in detail in the next quarterly report.

Under Subtask 1.3, initial captive particle image sequences were obtained for selected density fractions of two coals prepared in the laboratory of Professor Jack Crelling at Southern Illinois University (SIU). This work is part of the collaborative effort with SIU and Imperial College on coal heterogeneity and its implications for carbon burnout prediction. The initial experiments were designed to understand the qualitative combustion mechanisms for coal particles of differing density and petrographic composition. The initial data provide information on: (1) swelling, (2) ash/carbon interactions, (3) physical transformations in the late stages of combustion (such as fragmentation and microscale densification), and (4) statistical variations in single particle burnout times. Particularly interesting are the images revealing nonuniform swelling in the inertinite-rich heavy fraction of the Middleburg coal. These results are being reviewed by the project team (Gibbins and Crelling) and will be reported in detail next quarter.

Combustion-Induced Char Carbon Crystalline Transformations

Recent work has identified thermal char deactivation as an important phenomenon affecting the degree of carbon burnout in coal combustion systems [Davis et al., 1994, Hurt et al., 1994]. An important mechanism of deactivation is the transformation of the chemistry and crystal structure of the carbonaceous matrix, particularly for bituminous and higher rank coals. As discussed in previous reports, the general phenomenon of thermal annealing of carbons is well established, but there are very little data for the short times of interest in combustion systems. The process time scale is believed to have a large effect on carbon structure and reactivity, as it determines the time available for structural rearrangements during carbonization (for solid precursors) or for gas-particle conversion (for gaseous precursors). As an example, the time scale of formation is believed to influence the structure of carbon blacks manufactured by various processes. Thermal black particles (particles that have been produced by a pyrolysis process) have a gross concentric structure with a single nucleation center, while furnace black particles (particles produced during an oxidative combustion process) that are formed over much shorter time scales, consist of polynuclear particles with multiple growth centers [Marsh et al., 1971]. For organic solid precursors, new experiments are needed to identify the carbon structures produced at high heating rates and short times.

Several previous studies have obtained evidence of carbon annealing over the short times scales of combustion processes, including studies by Smith and Tyler [1972] on semi-anthracite, Levendis and Flagan [1987] on polyfurfuryl alcohol carbons, Davis et al. [1994] on Illinois #6 coal chars, and Hurt et al. [1994] on residual carbon in fly ash from commercial coal-fired power stations. These studies establish the importance of the effect in certain cases, but do not provide a sufficient data base to understand the behavior for the range of solid fuels of industrial interest.

A number of techniques are available for probing the crystalline structure of carbons, including optical reflectance, X-ray diffraction, Raman spectroscopy [Johnson et al., 1986], and high

resolution transmission electron microscopy (HRTEM) lattice fringe imaging [Ban, 1972]. The first three techniques infer crystalline structural parameters from bulk measurements, while lattice fringe imaging with HRTEM provides a detailed picture of nanoscale structures. The explicit structural information provided by HRTEM is invaluable, but the technique suffers the disadvantage of extremely small sample sizes, making a statistically accurate quantitative description of the bulk structure difficult to obtain [Marsh and Crawford, 1982], especially for heterogeneous solid fuels.

In our previous quarterly reports, we presented two series of fringe images for partially combusted chars from Illinois #6, PSOC 1493D, and Pocahontas #3, PSOC 1508D coals. Biomass chars from switchgrass and southern pine have also been characterized in similar fashion by Wornat et al., [1994].[1] In this report we present results of HRTEM carbon structural investigations for two additional parent coals (PSOC-1507D, Beulah lignite and PSOC-1451D, Pittsburgh #8) undergoing combustion in the CCL. The report then considers the complete set of Sandia samples examined to date, drawing from previously published work on several projects, to present an overview of our knowledge on combustion-induced char carbon crystalline transformations and their implications for kinetics and carbon burnout.

Experimental

Partially combusted char samples were prepared as described previously [Hurt et al., 1994]. Briefly, the char samples were prepared in the CCL entrained flow reactor by combustion in 12 mol-% oxygen at a nominal gas temperature of 1600 K. The oxygen content was chosen to produce particle temperature histories and degrees of conversion that are comparable to those experienced by the Illinois #6 coal in the earlier experiments. Under these conditions, peak mean particle temperatures range from 1900 - 2000 K. Samples were collected at residence times of 47, 72, 95, and 117 msec, corresponding to bulk char carbon conversions of 0, 27%, 42%, and 50%. The char samples were ground and placed on a holey carbon grid for HRTEM analysis at Sandia New Mexico. Carbon structure is examined in the vicinity of particle edges, where the sample is thin enough to partially transmit the electron beam. A number of these edge regions (typically ten to fifteen) are examined, after which four to five representative regions are photographed in the fringe imaging mode at high magnifications (approximately 2,000,000 x). From these photographic prints, representative fields of view are selected and reproduced.

New results

Selected results for Pittsburgh #8 are shown in Fig. 1.1. The young char at 47 msec shows slight to moderate turbostratic order, which develops further over the course of char combustion. After 117 msec of combustion, approximately 65% of the char has been oxidized and the remainder has a well-developed turbostratic crystallinity comparable to that observed in the latter stages of Illinois #6 combustion [Davis et al., 1994].

Under the same set of conditions, Beulah lignite shows slight to moderate order in the young char (Fig 1.2), but no further structural development with increasing residence time. The initial

---
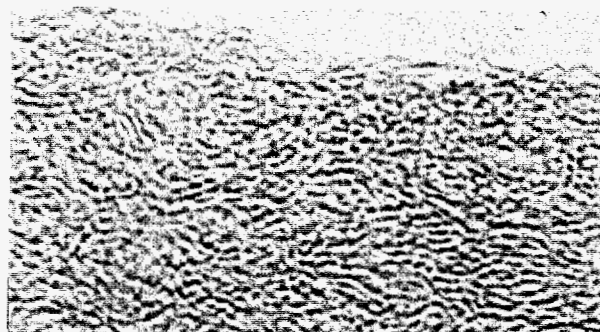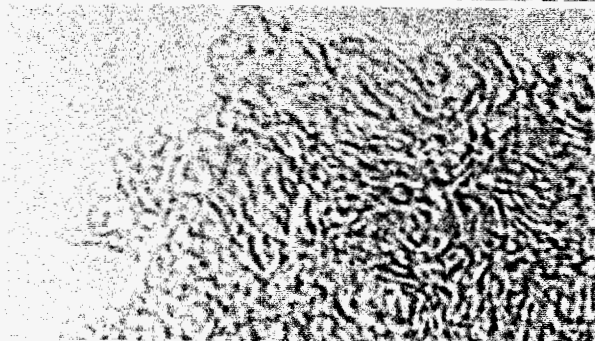
47 msec
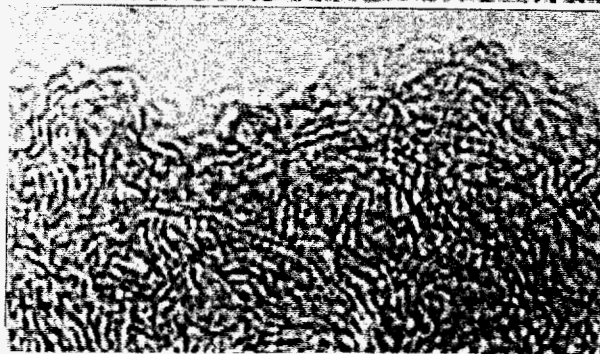
72 msec

117 msec

10 nm

Figure 1.1   Fringe images of partially combusted chars from Pittsburgh #8 coal showing the
development of turbostratic order during combustion. Combustion in 12 mole-
% oxygen at a nominal gas temperature of 1600 K.

47 msec
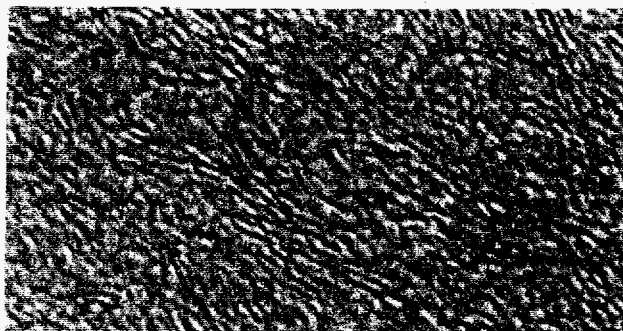
72 msec
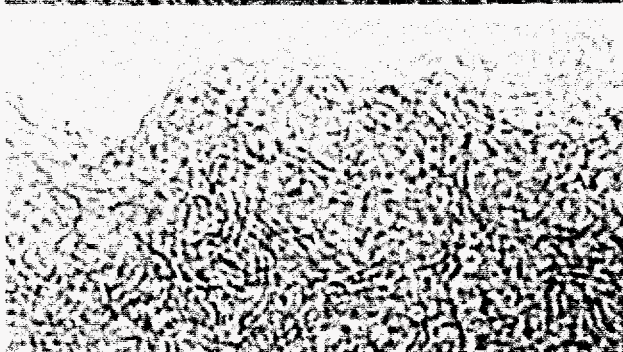
117 msec
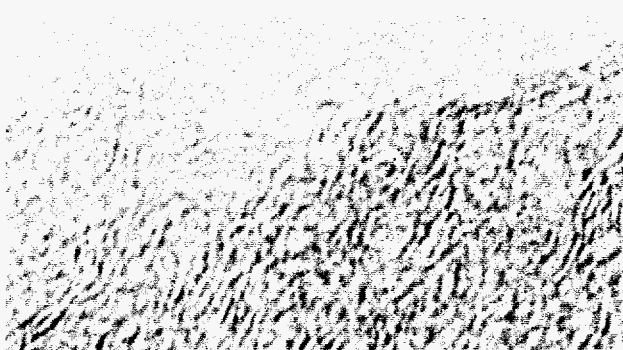
10 nm

Figure 1.2   Fringe images of partially combusted chars from Beulah lignite showing moderate turbostratic order established early in combustion. Samples were prepared in 12 mole-% oxygen at a nominal gas temperature of 1600 K.

structure is approximately frozen during the char combustion phase, as has also been observed for the biomass chars [Wornat et al, 1994]. For both Pittsburgh and Beulah chars, some, but not all, of the regions examined exhibited an overall anisotropy, or a statistical preference for common orientation of the layers. The frequency of these regions and the uniformity of the preferential orientation within the regions are much less than those observed for Pocahontas char [Hurt et al., 1994].

Figure 1.3 shows a region of concentric circular crystallinity that is a notable structural feature observed as a minority phase in the Beulah lignite sample. A number of these crystalline features are found in the Beulah lignite samples, but not in any of the other samples examined to date (for six parent fuels). The concentric structures are typically found in clusters, concentrated in only a few of the regions examined. These same regions tend to contain dark patches associated with inorganic inclusions, and in many cases, the dark patches overlap in space with the circular crystalline features. The coincidence of the dark patches and the crystalline carbon suggests that
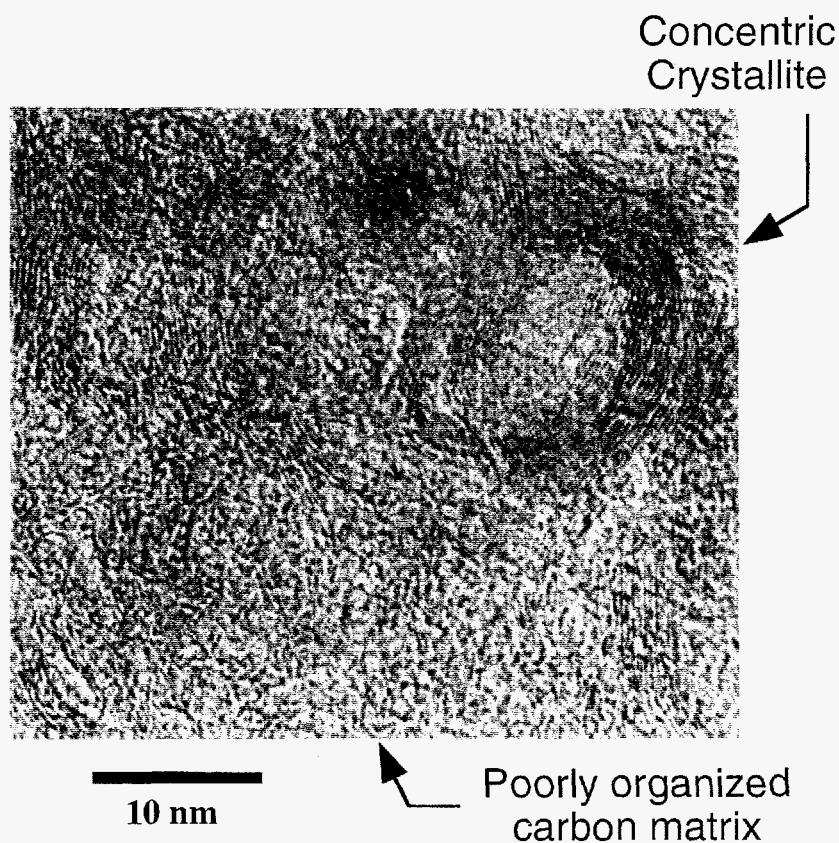
Figure 1.3   An example concentric crystalline structure observed as a minority phase in Beulah lignite char. Sample prepared by partial combustion for 117 msec in 12 mole-% oxygen at a nominal gas temperature of 1600 K. Dark patches in fringe image are believed to represent inorganic inclusions.

inorganic material is catalyzing the growth of the turbostratic phase or providing a nucleation site for crystal growth. The inorganic material probably arises from atomically dispersed mineral matter that has migrated and agglomerated during carbonization and heat treatment.

The circular region in Fig. 1.3 may be two-dimensional crystalline rings or, more likely, two-dimensional projections of three dimensional onion-like structures. Concentric carbon crystal structures have been observed in a number of other systems, in particular soot, carbon black, and the condensed products of from arc vaporization. A minority phase having concentric crystalline structure has also been observed in amorphous carbon films formed by vacuum deposition [Iijima, 1980]. These crystalline regions may represent distinct particles that nucleate from the gas phase in the vicinity of the vaporizing arc. Roughly spherical growth centers have also been observed in pyrocarbon coatings [Yust and Krautwasser, 1974].

Ugarte [1992] has demonstrated that quasi-spherical graphitic particles can be formed from the *condensed phase* by irradiating soot or amorphous carbon samples with a high intensity electron beam. In these experiments, soot from an arc vaporization process, some of which was in the form of nested graphitic tubules, spontaneously rearranges under the electron beam to form nested concentric spheres, or "buckyonions". Occasionally distinct crystalline growth centers are observed in graphitized coals [Ban, 1972].

Overall, the formation of concentric structures seems to be a natural feature of carbons produced from the gas phase through nucleation processes. In contrast, the formation of concentric structures in bulk solids may require the presence of impurities acting as nucleation sites. Figure 1.4 shows concentric crystallinity in carbonized microporous polymer foam containing small iron inclusions (the dark patches). The "crystallite" at the upper left of the image consists of over 20 nested graphitic loops surrounding an iron-rich core. Examination of a large number of such regions reveals that *each* distinct iron particle forms a growth center for concentric crystalline (or turbostratic) carbon. In addition, there are many concentric crystalline regions that are not clearly associated with iron particles. It is possible that these sites previously held iron particles that diffused or vaporized at some point during carbonization.

Similar metal/carbon structures have been observed by Ugarte [1994] during experiments in which a metallic salt or oxide is co-vaporized with carbon by an electric arc discharge. The condensed products contain a small percentage of concentric carbon crystallites surrounding a metal carbide core [Ugarte, 1994], similar in appearance to the sample in Fig. 1.4. Based on the above observations, it is likely that the well dispersed mineral matter in lignites acts as a catalyst for development of turbostratic order, either locally, affecting a small fraction of the sample, or throughout the structure.

Summary of behavior for various solid fuels

Table 1.1 summarizes the HRTEM observations of the combustion-induced crystalline transformations as a function of coal rank for chars from the six parent fuels examined to date. The nature of the carbon crystalline transformations is a pronounced function of the parent fuel,

Figure 1.4   Development of concentric carbon crystalline structures in Fe-doped polyacrylonitrile carbon foam.† Iron inclusions are often seen to be the nucleus for growth of the concentric crystallites.

† sample provided by William Even through Sandia's Engineered Microporous Materials Program.

with the extent of order decreasing with decreasing geologic age or oxygen content.of the parent coal.[2] The low rank materials are disordered and maintain their disorder throughout combustion. The two high-volatile bituminous coals (Illinois #6 and Pittsburgh #8) undergo a transition from nearly amorphous to fully turbostratic during the char combustion stage. The development of turbostratic order in these two chars appears to correlate well with their loss of reactivity and early near-extinction, observed previously [Hurt, 1993]. The high-rank Pocahontas char shows a high degree of order after only 47 msec of residence time, suggesting an ordering process in the fluid stage of carbonization.

Table 1.1

Overview of Combustion-Induced Char Carbon Crystalline Transformations as a Function of Rank

			increasing rank --->			
Precursor	Southern Pine	Switchgrass	Beulah lignite	Illinois #6	Pittsburgh #8	Pocahontas #3
PSOC #			1507D	1493D	1451D	1508D
Extent of Char Crystallinity	low	low	moderate	low->high[†]	moderate->high[†]	high
Degree of Anisotropy	none	none	moderate	none	slight	high
Timing of the Structural Rearrangements	--	--	(early)	during char combustion	during char combustion	early (in fluid phase)

[†] increasing with residence time during char combustion

Role of chemical composition. The rank-dependent behavior in Table 1.1 is similar to that observed in conventional carbonization experiments at low heating rates. In low-rank materials, oxygen serve as a cross-linking agent that prevents rearrangement of the graphitic basic structural units. Hydrogen act in the other sense, capping free radicals at the edges of the units and thus

---

[2] A partial exception to this observation is the higher degree of order observed in the youngest lignite char (47 msec) compared to the youngest (47 msec) Illinois #6 char. The rapid development of discernible order in lignites may be due, in part, to a catalytic effect of inherent mineral matter in the particle or to the slightly higher particle temperatures (by 50 - 100 K) achieved during lignite combustion. Slight differences in temperature may be significant in light of the highly non-linear nature of crystalline rearrangements. For example, Ban et al. [1975] observe very little structural rearrangement during carbonization of polyvinylidene chloride (PVDC) between 1273 and 1573 K, but a significantly more ordered structure after further heat treatment to 1973 K. This result implies the presence of a threshold temperature, above which bond breaking and rearrangements proceed rapidly.

inhibiting crosslinking and promoting fluidity. As a function of rank, both fluidity and the propensity for structural ordering reach maxima for the low-volatile, bituminous coking coals, which have the highest H/O ratios.

Sulfur, being isovalent with oxygen, can also act as a crosslinking agent. Although sulfur content among coals varies more with source than with coal rank, there is evidence that the *forms* of organic sulfur show a systematic rank dependence. The ratio of aromatic to aliphatic sulfur forms increases with coal rank and with the degree of carbonization [Derbyshire, 1991]. Non-aromatic sulfur functionalities, such as sulfides and thiols, can participate in crosslinking reactions that stabilize the carbon matrix and impede further structural rearrangements. Some sulfur forms are refractory, persisting during carbonization up to temperatures in excess of 1700 C [Derbyshire, 1991].

Other systems show that a high degree of resistance to structural ordering include glassy carbons prepared from phenolic resins or from polyvinylidene chloride (PVDC) [Ban et al, 1975]. Although PVDC ($-CH_2CCl_2-$) does not contain oxygen as a crosslinking agent, turbostratic structural ordering is inhibited by the essentially non-aromatic nature of the polymer chains and by C-C crosslink formation during carbonization [Ban et al., 1975]. A higher degree of order has also been observed in chars from polyethylene chars than in cellulose-derived chars [Ban, 1972], possibly due to the oxygen content of cellulose .

Individual maceral behavior. The same line of reasoning used above is capable of rationalizing the deactivation behavior of individual macerals during high temperature heat treatment. Recently, Man et al. [1994], have observed inertinite to be more resistant to deactivation than vitrinite upon high temperature heat treatment. A vitrinite concentrate was observed to be more reactive than an inertinite concentrate after charring at 1000 C, but the trend was reversed as heat treatment temperature was increased above 1800 C. The inertinite chars are relatively resistant to thermal deactivation.

The behavior of vitrinite and fusinite (one of the most abundant inertinite macerals) can be compared by considering the two pathways in the coalification plot in Fig. 1.5. Path A represents coalification to vitrinite followed by carbonization in the laboratory. Because coalification has selectively removed oxygen, the hydrogen-rich vitrinite softens, undergoes nanoscale rearrangements, and deactivates readily upon heat treatment.

The most widely accepted theory for the origin of fusinite identifies it as fossil charcoal — the product of ancient forest fires. Inertinite is thus charred directly from the wood precursor and follows path B, a more nearly direct path that does not follow the coalification band [Fletcher and Hardesty, 1992]. This charring occurs while oxygen is abundant and the woody tissue does not soften or develop significant crystalline order [Wornat et al., 1994]. It partially carbonizes to form a disordered char-like material (fusinite) which may continue to evolve somewhat in the deposit over geologic time. When fusinite is carbonized in the laboratory, its low hydrogen content precludes fluidity and structural rearrangement, and it resists thermal deactivation. In a sense, the disorder present in the initial wood has been preserved — "sealed" into place by the early and rapid carbonization.
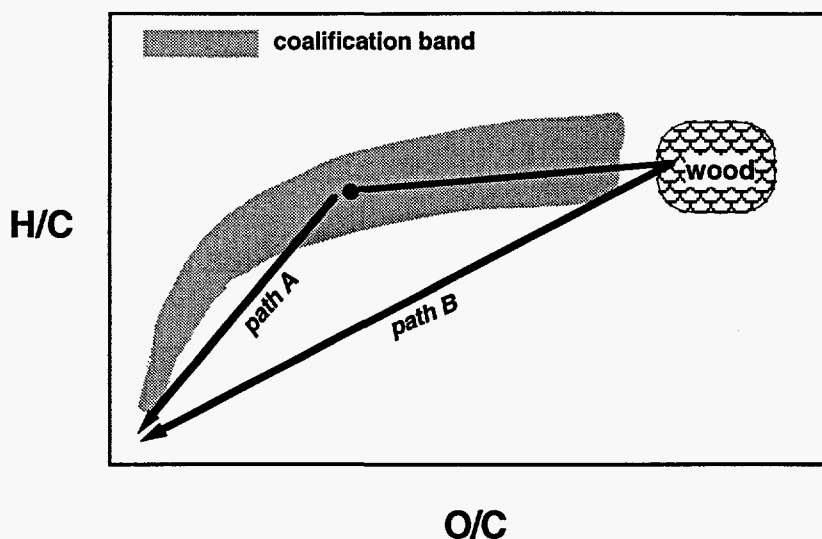
Figure 1.5   Coalification diagram showing formation/pyrolysis pathways for vitrinite (A) and fusinite (B) chars.

The resistance of inertinite chars to thermal deactivation helps to explain the observation that we made previously — that residual carbon samples extracted from the fly ash in utility boilers burning U.S. coals do not typically exhibit high concentrations of clearly identifiable unfused inertinite residues [Hurt et al., 1994b,c]. The high temperature heat treatment received in the furnace renders vitrinite-rich particles as unreactive as inertinite-rich particles, thus minimizing the enrichment of inertinite as combustion proceeds.[3]

Anisotropic structures. Many of the samples examined showed at least some statistical tendency toward preferential orientation of the graphitic layer planes. Preferential orientation is believed to promote deactivation, which involves the coalescence of neighboring graphitic units that must be first be approximately aligned. A high degree of anisotropy in the initial stages of carbonization is, in fact, a prerequisite for the ultimate production of high-quality synthetic graphite [Boulmier et al., 1982; Peters et al., 1991]. The high degree of anisotropy exhibited by the young Pocahontas char is likely the result of mesophase (liquid crystal) formation during the fluid phase of carbonization. It is remarkable that such long range order is observed after only 50 msec of combustion residence time. Anisotropic coke texture has been observed previously in products of rapid pyrolysis and combustion in the laboratory and in residual carbon from power plant fly ash using polarized light microscopy [Bailey, et al., 1990].

In some cases, preferential orientation can be a remnant of the bedding plane anisotropy in the parent coal. High rank coals (anthracites and low-volatile bituminous coals) are known to have organic structures that are anisotropic with preferred orientation of the aromatic layers parallel to the bedding plane [Roberts et al., 1991] and to produce anisotropic chars [Qian et al., 1983].

---

[3] Note that some inertinite persistence may still be observed due to the higher *density* of inertinite chars and thus the greater weight of carbon per unit particle volume and the longer burnout time for a given reactivity.

Anthracites retain their bedding anisotropy upon carbonization, and coking coals may to some extent as well [Qian et al., 1983]. Low and mid-rank coals in contrast are only slightly anisotropic at the molecular level [Roberts et al., 1991] and their chars are generally isotropic. Indeed, most nonfusible materials are isotropic, but exceptions exist due to solid-phase reordering [Bailey et al., 1990]. Overall, the various anisotropic structures observed here are the result of some combination of coal anisotropy with reference to the bedding plane, mesophase formation, and coordinated nanoscale rearrangements in the solid phase.

In summary, HRTEM analysis is providing extremely valuable insight into combustion and burnout behavior of a variety of solid fuels. Considering the entire set of Sandia samples examined to date, the degree of crystalline order appears to show a significant correlation with global oxidation reactivity. The trends observed by HRTEM lattice fringe imaging coincide with the trends in reactivity, both as a function of parent material (coal rank) and as a function of combustion history (carbon burnout). First, the ordered nature of the high rank chars correlates well with their low reactivities. Further, the observed propensity for higher rank chars to pregraphitize during char combustion is consistent with their propensity to undergo thermal deactivation and early extinction [Hurt, 1993, Hurt and Davis, 1994]. Low rank materials maintain their disordered structures throughout high conversion, and this parallels the recent observation of late extinction events for lignites and biomass chars [Hurt et al., 1994].

PLANS FOR NEXT QUARTER

The high conversion data from the hot-walled reactor experiments has been analyzed and will be is presented and compared to global model predictions in the next quarterly report. Progress will also be made next quarter on the formulation and testing of a char deactivation submodel. Additional captured particle imaging (CPI) experiments are planned on the density fractions supplied by the laboratory of Professor John Crelling at SIU. Progress will also be made on the upgrade of the CCL computer and electronics systems.

ACKNOWLEDGMENTS

PUBLICATIONS, PAPERS, AND PRESENTATIONS

A paper derived from PETC-sponsored research was submitted this quarter for publication in *Energy and Fuels*. The reference is given below.

Baxter, L. L., Mitchell, R.E., Fletcher, T.H., and Hurt, R.H., "Nitrogen Release During Coal Combustion" submitted to *Energy and Fuels*, November 1994.

A presentation was also given at the Annual Meeting of the AIChE in San Francisco entitled "Carbon Densification Mechanisms in Combustion," which incorporated PETC sponsored work on unburned carbon and combustion-induced char crystalline transformations.

REFERENCES

Bailey J.G., Tate, A., Diessel, C.F.K., and Wall, T.F. *Fuel* 69 225 (1990).

Ban, L.L. in *Surface and Defect Properties of Solids — Volume 1* (Specialist Periodical Reports) The Chemical Society, London, 1972

Ban, L.L. *J. Appl. Cryst.* 8 415 (1975).

Boulmier, J.L, Oberline, A., Rouzaud, J.N., and Villey, M. *Scanning Electron Microscopy* 1523-1538 SEM Inc. AMF O'Hare, Chicago, IL, 1982.

Buseck, P.R., Bo-Jun, H., *Geochimica et Cosmochimica Acta* 49 2003 (1985).

Busek, P.R., Bo-Jun, H., and Keller, L.P. *Energy and Fuels* 1 105 (1987)

Davis, K. A., Hurt, R. H., Yang, N. Y. C., and Headley, T. H., "Evolution of Char Chemistry, Crystallinity, and Ultrafine Structure during Pulverized Coal Combustion," accepted for publication in *Combustion and Flame*, 1994.

Derbyshire, F., *Fuel* 70 276 (1991)

Even, W. personnal communication, 1994

Fletcher, T.H. and Hardesty, D.R. *Compilation of Sandia Coal Devolatilization Data, Milestone Report*, SAND92-8209, May (1992)

Hurt, R. H. "Reactivity Distributions and Extinction Phenomena in Coal Char Combustion" *Energy and Fuels* 7 721-733 (1993)

Hurt, R. H. and Davis, K. A., "Near-Extinction and Final Burnout in Coal Combustion," accepted for publication in the *Proceedings of theTwenty-Fifth (International) Symposium on Combustion,* 1994

Hurt, R. H. and R. E. Mitchell. "Unified High-Temperature Char Combustion Kinetics for a Suite of Coals of Various Rank" *24th International Symposium on Combustion*, The Combustion Institute, Pittsburgh, PA, pp. 1243 - 1250 (1992)

Hurt, R. H., Davis K. A. and Hardesty, D. R. in *Coal Combustion Science--Quarterly Progress Report,* Hardesty, D. R. (ed.), Sandia Technical Report, June - September (1994).

Hurt, R.H., Davis, K. A., Yang, N.Y.C., and Gibbins, J. R. "Carbon Burnout in Pulverized Coal Combustion: An Overview of Mechanisms and Trends," *Fourth International Conference on the Effects of Coal Quality on Power Plants*, August 1994b.

Hurt, R. H., Davis, K. A., Yang, N. Y. C., and Headley, T. R. "Residual Carbon from Pulverized Coal Fired Boilers 2: Morphology and Physicochemical Properties, accepted for publication in*Fuel*, May 1994c.

Iijima, S. *Journal of Crystal Growth* 50 675 (1980)

Johnson, C. A., Patrick, J. W., and Thomas, K. M., *Fuel*, 65 1284 (1986).

Levendis, Y.A. and Flagan, R.C. *Carbon*, 27:265 (1989).

Man, C.K., Beeley, T.J., Gibbins, J.R., Lockwood, F.C., Williamson, J., Crelling, J.C., and Hurt, R.H. "Reactivity Measurements on Chars Formed at Combustion Temperatures—The Key to Burnout Prediction?" *Fourth International Conference on the Effects of Coal Quality on Power Plants,* August 1994.

Marsh, H., and Crawford, D., *Fuel* 61 876 (1982)

Marsh, P.A., Voet, A., Mullens, T.J., and Price, L.D. *Carbon* Vol. 9, pp. 797-805 (1971)

Peters T.J., Jenkins, R.G., Scaroni, A.W., and Walker, P.L.Jr. *Carbon* 29:7 981 (1991)

Qian, Z., Clarke, D., and Marsh, H. *Fuel* 62 1084 (1983).

Roberts, J.E., Coleman, K.M., Alaimo, M.H., and Larsen, J.W. *Energy and Fuels* 5:5 619 (1991)

Smith, I.W. and Tyler, R.J. *Fuel* 51 313 (1972)

Ugarte, D. *Nature* 359 707 (1992).

Ugarte, D. *Materials Research Society Bulletin*, 19:11 39 (1994)

Wornat, M. J., R. H. Hurt,, N . Y. C. Yang, and T. J. Headley, "Structural and Compositional Transformations in Biomass Chars during Combustion" accepted for publication in *Combustion and Flame*, 1994.

Yust, C.S., Krautwasser, H.P. *Carbon* 13 125 (1975)

PROJECT TITLE: COAL COMBUSTION SCIENCE

                                      TASK 2: DEPOSIT GROWTH AND PROPERTY
                                              DEVELOPMENT IN COAL-FIRED
                                              FURNACES

ORGANIZATION: Sandia National Laboratories, Livermore

CONTRACT: FWP 0709

REPORTING PERIOD: October 1 - December 31, 1994

REPORTED BY: L. L. Baxter and D. R. Hardesty

                                    Phone: (510) 294-2862 and (510) 294-2321

OBJECTIVES FOR TASK 2

Task 2 is a four-year project (October 1993 - September 1997) focused on the growth and properties of deposits generated in coal-fired furnaces. The objectives of this project are: (1) to provide a self-consistent database of simultaneously measured, time-resolved, ash deposit properties in well-controlled and well-defined environments and (2) to provide analytical expressions that relate deposit composition and structure to deposit properties of immediate relevance to PETC's Combustion 2000 program. This project is distinguished from related work being done elsewhere by: (1) the development and deployment of *in situ* diagnostics to monitor deposit properties, including the heat transfer coefficient, porosity, emissivity, tenacity, strength, density, and viscosity; (2) the time resolution of such properties during deposit growth; (3) simultaneous measurement of structural and composition properties; (4) development of algorithms from a self-consistent, simultaneously measured database that includes the interdependence of properties; and (5) application of the results to technologically relevant environments such as those being planned under the Combustion 2000 program.

Work completed during FY94 emphasized diagnostics development. During FY95, this development work will be completed and we will emphasize application of the diagnostics to meet the other project objectives. Included in this work are the development and application of two diagnostics systems for monitoring, *in situ* and in real-time, the properties of inorganic materials on heat-transfer surfaces and in the gas-phase during controlled combustion of selected coal samples in Sandia's Multifuel Combustor (MFC). Other diagnostics are being incorporated into the MFC that will eventually be used to characterize ash deposit properties.

The project comprises six subtasks, as follows:

Subtask 2.1 Diagnostics for Coal Combustion Environments

The objective of this subtask is to develop and demonstrate diagnostics capable of *in situ* measurement of: (1) condensed-phase species on surfaces in combustion environments and (2) inorganic vapors in turbulent, particle-laden, combustion gases.

Subtask 2.2 Experimental Determination of Transport, Thermal, and Structural Properties of Ash Deposits

The objective of this subtask is to provide self-consistent, simultaneous measurement of ash deposit properties under combustion conditions that simulate commercial-scale environments such as those expected to occur in Combustion 2000 technologies. Properties to be measured simultaneously and in real time include thermal conductivity, emissivity, porosity, mass and volume rate of growth, surface composition, and tenacity. Additional properties to be measured, but not in real time or *in situ*, include bulk elemental composition, bulk species composition, shear strength, true density, and detailed morphology.

Subtask 2.3 Analysis of Deposit Properties

The objective of this subtask is to provide an analytical capability for describing the development of deposit properties in combustion systems. Deposit properties to be predicted by this analytical method are similar to those discussed in Subtask 2.2 and include: (1) thermal conductivity, (2) emissivity, (3) porosity, (4) mass and volume rate of growth, (5) surface composition, (6) tenacity, (7) bulk elemental composition, and (8) major species composition.

Subtask 2.4 Chemical Reactions in Deposits

The objective of this subtask is to determine rates and mechanisms that describe chemical reactions in coal ash deposits that alter their properties or their morphology. This subtask is more limited in scope than the previous subtasks. We do not intend to conduct a comprehensive study of inorganic chemistry as it relates to ash deposits. We do intend to review available literature and perform calculations that allow us to capture the first-order terms that describe changes in deposit chemistry with time. This work will result in usable results, but is limited to global kinetics and simplified chemical mechanisms that outline the nature of the reactions and their dependence on operating parameters. The details of the kinetics will not be determined.

Subtask 2.5 Application to Combustion 2000 Program

The objective of this subtask is to exchange technology developed under other subtasks with ongoing Combustion 2000 efforts by other PETC contractors.

Subtask 2.6 Documentation

The objective of this subtask is to provide timely and accurate documentation of project progress, major milestones, and publishable results.

SUMMARY OF TECHNICAL PROGRESS DURING THIS QUARTER

Subtask 2.1   Diagnostics for Coal Combustion Environments

Significant progress was made this quarter on the development of the tunable diode laser for analysis of alkali vapors in the gas phase and on application of the FTIR emission spectroscopy diagnostic to analyze chemical changes in deposit compositions. These subjects are discussed separately below.

Tunable Diode Laser Spectroscopy

Summary

During this quarter, the tunable diode laser (TDL) was successfully used to detect a portion of an alkali vapor (NaCl) spectrum. These are the first definitive measurements of alkali-bearing vapors in MFC-related equipment. Figure 2.1 illustrates one of the spectra collected this quarter that exhibits a major feature and several minor features. Both ordinates are linearly proportional to signal strength but are in otherwise arbitrary units. The abscissa is approximately linearly proportional to wavenumber over the approximate range from 377.5 to 378 cm^{-1}, but the wavenumber calibration has not yet been performed. The dashed line referenced to the right represents the absorbance spectrum of sodium chloride.

The remainder of this section describes the details of electrical and optical components of the system, collecting the spectrum, and analyzing the results.

System Description

A tunable diode laser probes the vibrational spectrum of alkali-containing vapors such as chlorides, hydroxides, and sulfates of sodium and potassium. The vibrational bands for the hydroxides and chlorides are in the region from 330 to 400 cm^{-1} (30 to 25 μm), a region requiring more specialized equipment than is common for most molecular spectroscopy. Figure 2.2 illustrates the major components of this system.

A tunable diode laser (TDL) provides the probe beam for analyzing the vapors. This lead-salt diode operates at low temperature (7-35 K), and is less well behaved than traditional TDLs. A Laser Photonics cryogenic (helium) compressor and cold finger maintains the laser temperature at a set value. The cold finger can accommodate up to four diode lasers simultaneously. Three are currently installed, but all of the data reported below were collected with a single diode.

The laser is tuned over a range of about 0.5 cm^{-1} by varying the diode current between its lower threshold value (typically $\approx$ 100 mA) and its upper limit (typically 500 mA to 1 A). The lower limit is dictated by the current required to induce lasing in the diode. The upper limit is dictated by the safe current carrying capacity of the laser. The specific frequency of the laser light is determined by a combination of temperature and current. In practice, these diodes emit approximately twelve frequencies simultaneously, depending on current and temperature. The beams from the laser are

more divergent than is common in most lasers. The beams are collimated with an off-axis paraboloidal mirror, but they still diverge somewhat. The beam is chopped either by chopping the current to the diode or by passing the beam through a mechanical chopper. Beam chopping has a practical upper limit of around 5 kHz. The current controller installed with the TDL has a maximum current modulation rate of 1 kHz, but more rapid modulation can be controlled by interfacing the controller with external signal generators.

The beam then passes through a furnace used to generate reference, test, and calibration spectra. This furnace operates at temperatures up to about 1600 °C and is open at both ends. A version with windows is being developed to allow lower pressure (20 Torr), more controlled, calibration
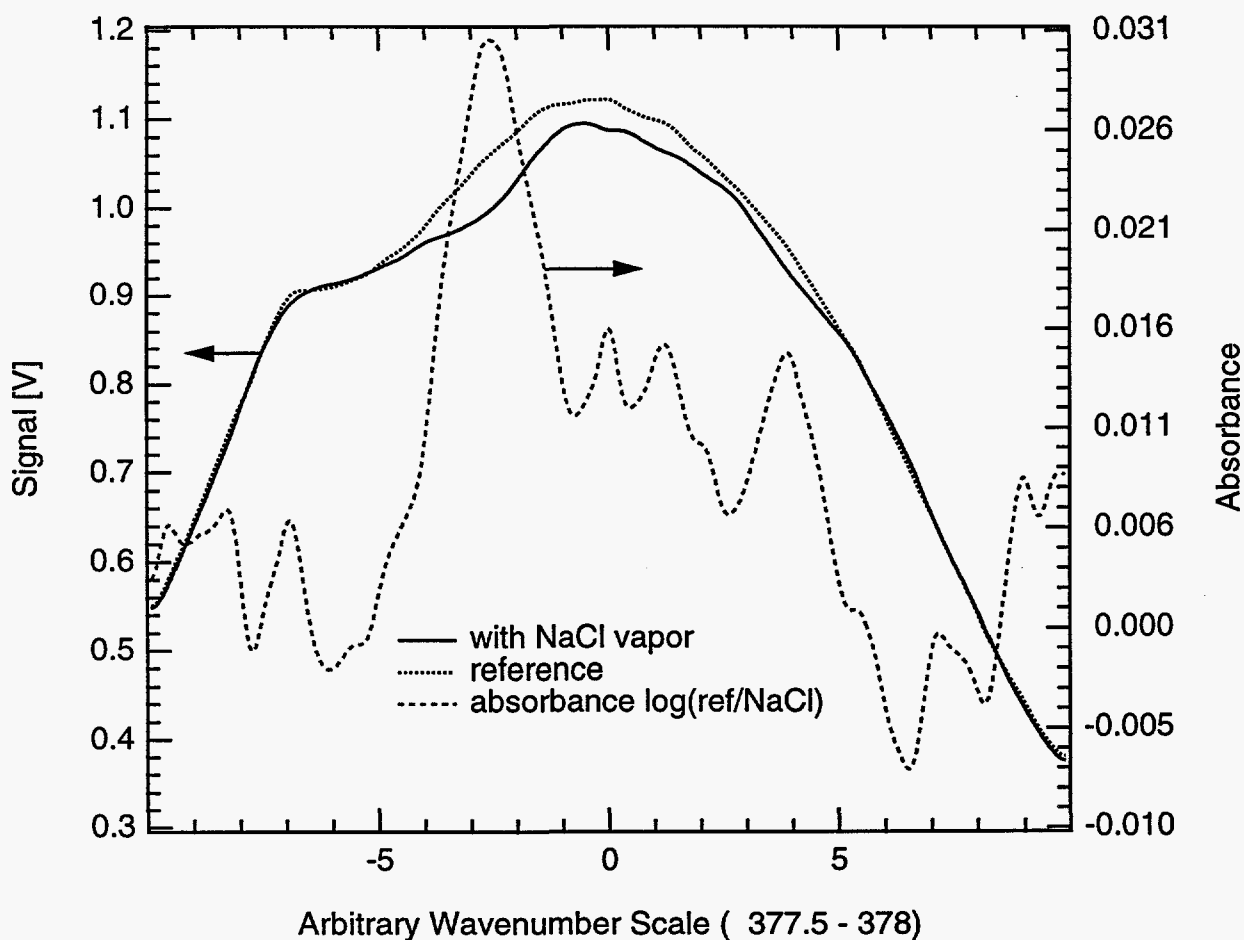
Figure 2.1   Reference and probe signals, together with absorbance spectrum, for the portion of the NaCl spectrum between approximately 377.5 and 378 wavenumbers.
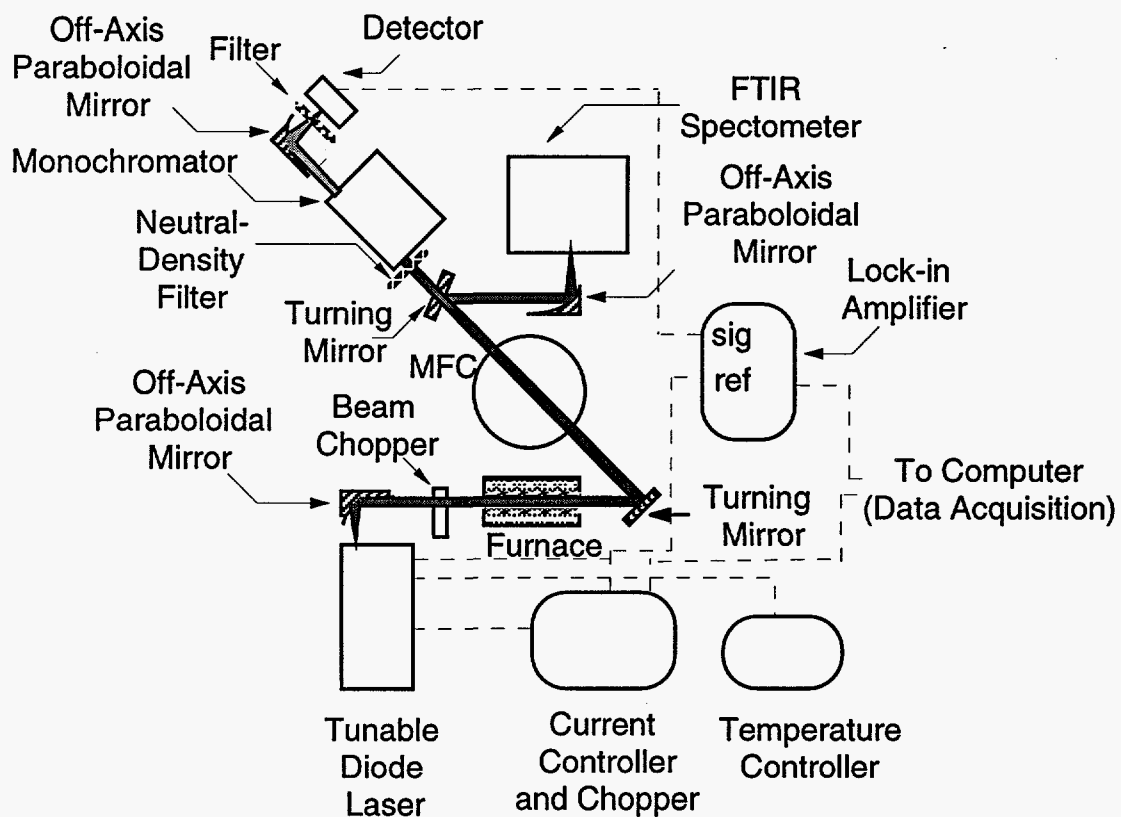
Figure 2.2   Schematic diagram of the TDL system used to monitor alkali-containing vapors. Optical components are illustrated as rectangles. Electronic components are illustrated with rounded corners.

data to be obtained. The material of choice for these windows is thallium bromoiodide, generally referred to as KRS-5. Its advantages include its transparency at these wavelengths and reasonable transparency at visible wavelengths. Traditional infrared materials such as potassium bromide and sodium chloride are opaque at the wavelengths we are interested in (25-30 μm). Means of placing KRS-5 windows on either end of the furnace are still being pursued. The windows must be maintained at relatively cool temperatures, well under 100 °C for both physical and safety reasons. Thallium bromoiodide softens at low temperature and is toxic. There are known ways to protect the windows from heat or condensing inorganic vapors, while providing an gas-tight seal for the furnace, but they require both composition and temperature gradients in the test cell. The furnace walls are removable and are composed of available ceramic materials, generally either mullite or silicon carbide.

After exiting the furnace, the beam is directed through the test section of the Multifuel Combustor (MFC). Significant beam steering is induced by index of refraction gradients in both the furnace and the MFC test section. The MFC has added complexities of particle interference and turbulent

fluctuations in gas temperature and composition. Measures have been taken to minimize the impacts of these issues by using modulated signals and lock-in amplifier detection, averaging scans both in real time and by repeated experiments, and shielding the detector from stray radiation.

During laser calibration and testing, a turning mirror directs the beam to a BioRad FTS-40/60 FTIR spectrometer. The spectrometer is useful for verifying that the laser is operating and for identifying the approximate frequency of the laser beams. However, it has a maximum resolution of 0.1 cm^{-1}, with a more practical limit being 1 cm^{-1}. This compares with a laser line width of about 0.0001 cm^{-1} and a tuning range of about 0.5 cm^{-1}. The FTIR spectrometer is only marginally capable of resolving the tuning range and determining the absolute wavenumber location of the laser beams at various temperatures.

When spectra are collected, the turning mirror for the FTIR interferometer is removed and the laser passes through a neutral density filter (wire mesh) and into a monochromator. The filter is used to adjust beam intensity to be no more than 85% of detector saturation (10 V). The monochromator is used to select which laser mode from the TDL is detected and to discriminate against background radiation from the furnace and the MFC. Removal of the unneeded laser modes from the laser beam is indicated in Figure 2.2 by a change in the pattern used to represent the laser beam path. The wavenumber resolution of the monochromator is intentionally maintained at a low value (≈ 1 cm^{-1}) because the beam is tuned over a range of wavenumbers, all of which must pass through the monochromator. Both entrance and exit slits in the monochromator have been removed, with the apertures of the optics providing the approximate 1 cm^{-1} resolution. The monochromator, in its original form, was incapable of operating in the wavenumber region of emitted by these TDLs. An appropriate grating (18 µm, 150 lines/inch) was installed, but the automated controller and sine-drive mechanism were incapable of turning the grating as far as is required for work in the 330-400 cm^{-1} region. Physical modifications to the monochromator yielded acceptable results, but requires an artificial adjustment to the readings on the automated controller. The relationship between the indicated and actual wavelengths, together with data validating the accuracy of the changes, are illustrated in Fig. 2.3.

The laser beam terminates on a copper-doped germanium detector. This detector operates at liquid helium temperature and is contained in a dewar system. Its low operating temperature (≈ 4 K) is not trivial to maintain, and its sensitivity to temperature variation is strong. Cold, broad-bandpass filters in front of the detector are used to further reduce contributions from stray radiation sources.

The laser beam is chopped to help discriminate against stray sources of radiation and to accomodate the AC-coupled detector. The signal from the detector is passed through a lock-in amplifier together with the chopper reference frequency. The laser is scanned at a rate of about 0.01 Hz over a range of approximately 200 mA (current, rather than temperature, is used to tune the laser). The current can be increased, decreased, or alternately increased and decreased from its set point.

The detector output and a reference signal related to the laser current are recorded as a function of time by a computer data acquisition program. Typically, five to ten scans of the laser are averaged to produce the final spectra. The analysis of these scans and production of the ultimate spectra are discussed separately.
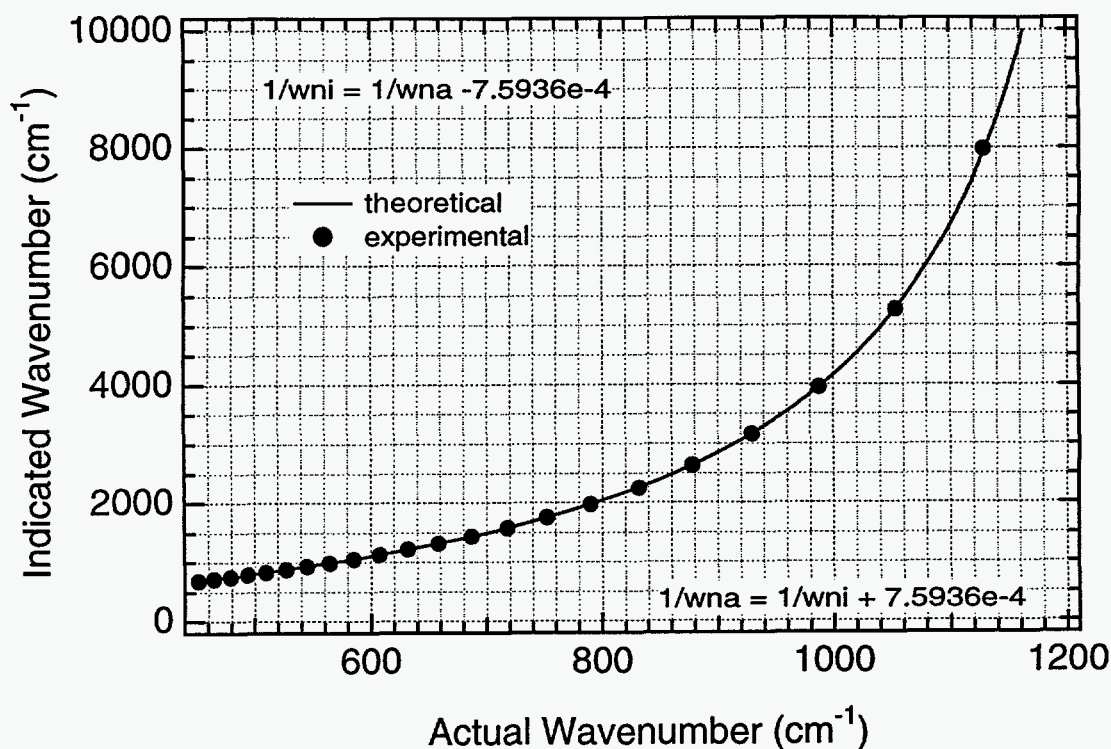
Figure 2.3 Adjustment of monochromator reading after physical modifications to allow use in the region of interest to NaCl spectroscopy. Experimental data are successive modes from a HeNe alignment laser. Equations represent theoretical adjustment, where wna is the actual wavenumber and wni is the wavenumber indicated by the monochromator.

Data Analysis

Data analysis is being done in collaboration with Prof. Peter Bernath at the University of Waterloo and Dr. R. S. Ram of the University of Arizona. At Waterloo, Bernath completed preliminary experiments to determine the spectral signature of alkali vapors using a high-resolution FTIR spectrometer. As noted in our previous quarterly, Bernath also contributed during the last quarter as a visiting scientist in our laboratory. Ram provided critical assistance in the reduction of these data. Both continue to contribute to the work being done under this subtask. Table 2.1 indicates some of the assignments resulting from this work. Indicated in the table are the wavenumber locations, peak heights, peak widths, and damping parameters of the principal peaks in the NaCl spectrum as experimentally determined in Prof. Bernath's laboratory.

Measured spectra were fit to Voigt profiles to determine these parameters. The Voigt profile represents a combination (convolution) of the Lorentzian and Gaussian profiles. Lorentzian profiles are used to represent lines broadened by intermolecular collisions, natural radiative decay, and saturation (population transfer to higher or lower energy states). Lines are broadened

homogeneously when every molecule is capable of emitting radiation at each frequency within the line width. Gaussian profiles are commonly used to describe inhomogeneously broadened lines by mechanisms such as Doppler broadening. Lines are broadened inhomogeneously when individual molecules cannot absorb or emit radiation at all frequencies within the line width. Rather, each molecule absorbs and emits radiation over a slightly different spectral range.

The spectra from which the parameters in Table 2.1 are derived were collected at a resolution of 0.01 cm^{-1}. The molecular linewidths are nearly an order of magnitude smaller than those indicated in the table. Under these conditions, the instrument lineshape also influences the observed lineshapes. The instrument lineshape for an FTIR spectrometer with no apodization is $\text{sinc}(x)$ $(\sin(x)/x)$. The combination of the incompletely resolved nature of the lines, signal to noise ratio, and interference and overlap between the peaks reduces the interpretation of the lineshape parameters indicated in Table 2.1 to fitting parameters. They should not be over-interpreted to suggest mechanisms of molecular interaction and radiative exchange.

The peaks form a bandhead, indicated by decreasing peak separation with increasing wavenumber, with the last resolvable peak located at approximately 387.84 cm^{-1}. This bandhead is possibly the most easily distinguished feature of the spectrum and it may be used to detect the presence of NaCl in the gas phase. The remaining spectrum includes peaks at wavelengths well below those indicated in Table 2.1. This bandhead and some of the peaks at lower wavenumbers will be probed by our laser diode to determine NaCl concentrations. As seen in the table, the linewidth of these peaks averages about 0.02 cm^{-1} under the conditions in which they were measured (temperature ≈ 1000 °C, total pressure ≈ 20 Torr). However, these widths are dominated by instrumental contributions. The actual linewidth of these peaks is approximately 0.002-0.003 cm^{-1}. Under the conditions used in the TDL experiments (temperature ≈ 1050 °C, total pressure $= 1$ atm), the line width is dominated by collisional (pressure) effects that scale linearly with pressure, resulting in widths of approximately 0.1 cm^{-1}.

Spectral features from other alkali-containing compounds (hydroxides and sulfates) are located at higher wavenumbers. They will be investigated later. Spectroscopy at higher wavenumbers can often be accomplished with liquid-nitrogen-cooled or even room-temperature equipment and does not involve many of the complexities inherent in liquid-helium-cooled equipment.

Results

The lock-in amplifier selects the time-varying component of the laser signal, as recorded in Fig. 2.4. The figure illustrates results from varying the current in both directions from a central setpoint nine times. Ideally, the signal would be perfectly periodic. In many cases, the detector sensitivity drifts during the experiment. An extreme example of this is shown by the data in Fig. 2.4. The drift is approximately linear with time and can be corrected to first order by normalizing it by a linear function as follows

$$S_n = \frac{S_m}{(p - p_1)\dfrac{(S_{m2} - S_{m1})}{(p_2 - p_1)} + S_{m1}} \tag{2.1}$$

Table 2.1

Results of Voigt profile fits to experimentally determined profiles of NaCl vapor.

Wavenumbers (cm^{-1})	Peak Height (arbitrary)	Peak Width (cm^{-1})	Shape Parameter: (1 = Gaussian; 0 = Lorentzian)
384.19965	0.0234	0.02151	0.6262
384.36442	0.0233	0.01994	1
384.52593	0.026	0.01818	1
384.6839	0.0199	0.02078	0
384.98813	0.0246	0.02122	1
385.13459	0.0199	0.01854	0
385.27727	0.0234	0.01839	0.7434
385.41665	0.0252	0.01946	1
385.55126	0.0197	0.02941	0
385.68167	0.0227	0.01898	1
385.8085	0.0193	0.01967	0
385.93261	0.0177	0.01792	0
386.05278	0.022	0.01881	0.5845
386.16942	0.022	0.01654	0.3743
386.2817	0.0244	0.0144	0.8195
386.38906	0.0198	0.01654	0
386.49488	0.0215	0.025	0.1
386.59546	0.0186	0.01504	0
386.69214	0.017	0.01673	0
386.78716	0.0159	0.025	0.1
386.87494	0.0187	0.01815	0.6942
386.96113	0.0173	0.01882	0.3007
387.0411	0.0155	0.01908	0
387.11862	0.0188	0.025	0.1
387.19243	0.0138	0.02167	0
387.26182	0.0153	0.01453	0
387.3286	0.0121	0.01867	0
387.39099	0.0143	0.02195	0.863
387.45007	0.017	0.025	0.1
387.50365	0.014	0.02563	0
387.55407	0.0146	0.02824	0.8318
387.59952	0.0145	0.02378	0
387.64089	0.0173	0.02363	0.6317
387.67982	0.0153	0.02055	0.3458
387.71382	0.0175	0.02094	0.6948
387.74517	0.0185	0.0205	0.6655
387.7719	0.0177	0.01844	0.4708
387.79427	0.0169	0.01713	0
387.81093	0.0159	0.0139	0.9233
387.82742	0.0278	0.0219	0
387.84063	0.0412	0.01129	0

where S_n and S_m represent the normalized and measured signals, respectively, p represents point number or time, subscripts 1 and 2 represent two normalizing positions in the time-resolved data. In the data analyses that follow, positions 1 and 2 are taken as the first and last peak in the time-resolved signal.
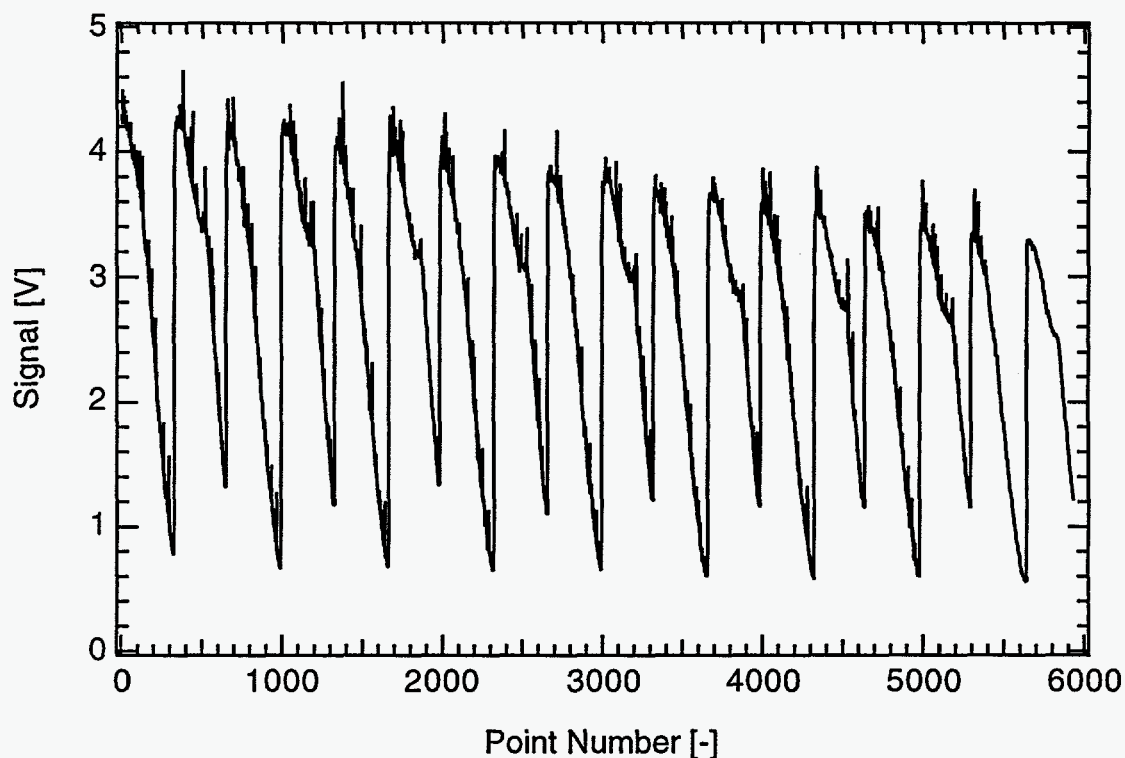

Figure 2.4   Peak-to-peak magnitude of the modulated laser intensity as a function of time (point number) from the scanning and modulated tunable diode laser. An extreme drift in detector intensity is seen as the declining magnitudes of the peak and valley heights with increasing point number.

The current passing through the diode is recorded simultaneously with the signal. After normalization, the laser intensity is recorded as a function of frequency, as illustrated by the data in Fig. 2.5. As indicated in the figure, there are over 5000 points recorded for the reference beam in total. The outliers seen at abscissa values of ±10 and 0 result from resetting the current in the diode to its central value during tuning. Data acquisition continues as the laser current is manually reset, resulting in spurious signals. These are removed from subsequent analyses. The remaining data are far more dense than is required to resolve the features of the spectrum we are seeking. They were averaged to improve signal-to-noise ratios resulting in the smooth curves illustrated in Fig. 2.6. A similar procedure was repeated with NaCl vapor in the beam. The vapor was generated by the furnace with a wall temperature of about 1050 °C, although the gas temperatures decreased axially due to heat losses and small convective currents though the furnace. The

logarithm of the ratio of the two signals represents the absorbance spectrum of NaCl, as illustrated in Fig. 2.6.
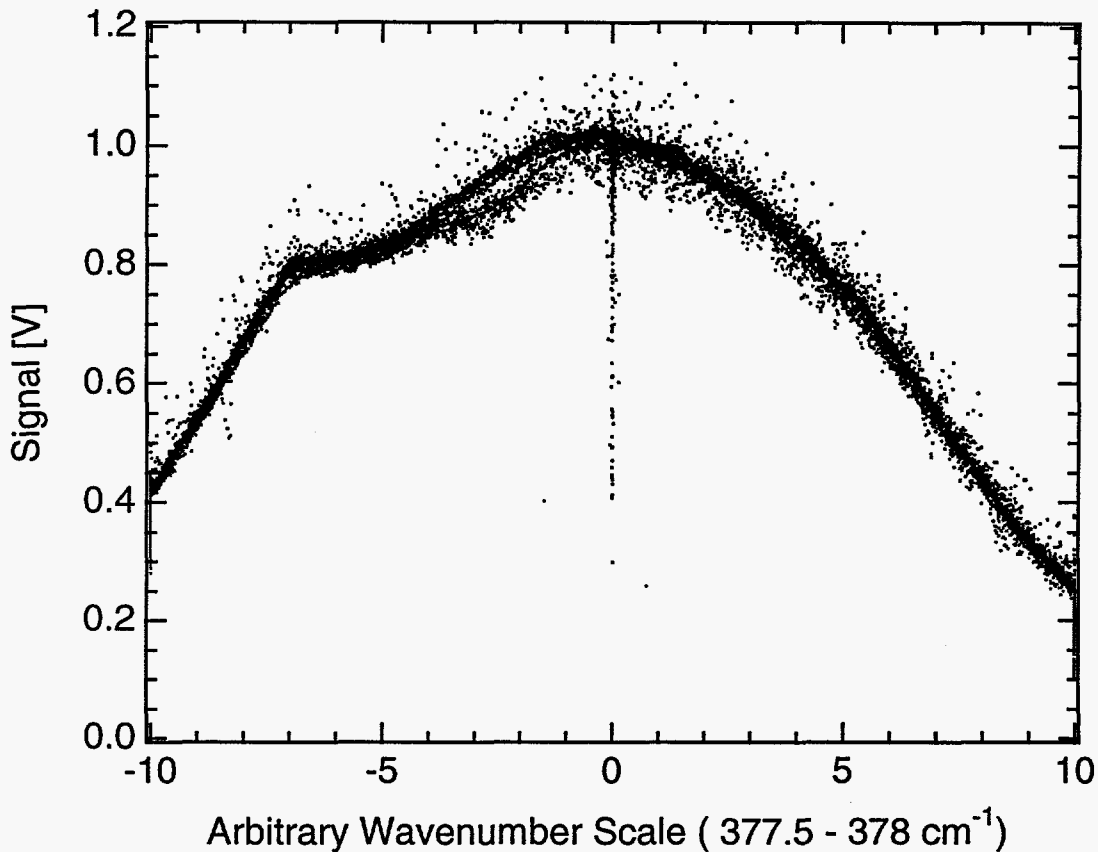
Figure 2.5   Data from reference and signal beams for NaCl experiments after normalization. There is an obvious difference in the signals at an abscissa value of about -3. The outliers at abscissa values of ± 10 and 0 are artifacts related to laser tuning and data acquisition and are removed in subsequent analyses.

The wavenumber values for the data in Figs. 2.5 and 2.6 have yet to be precisely determined. They correspond approximately to 377.5 to 378 cm^{-1} over the range of abscissa values illustrated in the figures. The features of the spectrum are consistent with this region of the NaCl spectrum, as determined by FTIR emission data collected by Bernath, after accounting for the effects of pressure and temperature differences. In Fig. 2.6 the peak at an abscissa value of about -3 corresponds to two overlapping peaks at approximately 377.8 cm^{-1} in the FTIR reference spectra. The minor peak at an abscissa value of about 4 corresponds to a second peak in the reference spectrum at about 377.95 cm^{-1}. A third peak in the reference spectrum centered at about 378.08

Figure 2.6 Reference and signal beams for the portion of the NaCl spectrum between
approximately 377.5 and 378 wavenumbers, together with the absorbance
spectrum. The major peak is located at approximately 377.8 cm^{-1}.

cm^{-1} may be responsible for the rise seen at the extreme high wavenumber end (abscissa value of 10) of the data. The peak separations and widths are consistent with this interpretation. While the major peak at an abscissa value of -3 is clearly separated from the noise, the remaining peaks discussed above are only separated and the remaining features in the spectrum are not clearly distinct from the noise. An accurate wavenumber calibration of the instrument is required to make more definitive statements about the data. Prior to performing this calibration, there are several modifications to the system that should be made, as will be discussed shortly.

Similar procedures were used to explore the region near the bandhead indicated in Table 2.1 (387.84 cm^{-1}). One of the laser modes observed is located just above this region. The resolution and wavenumber accuracy of the FTIR spectrometer used to characterize the laser are insufficient to definitively determine whether the laser was capable of tuning over the bandhead region. The results of one attempt to detect the bandhead are illustrated in Fig. 2.7. At first glance, it appears

that the bandhead is well defined at an abscissa value of -9.2. However, the peak should be in the opposite direction to that indicated. This is most likely a consequence of the abrupt decrease in laser intensity at the lower current threshold.
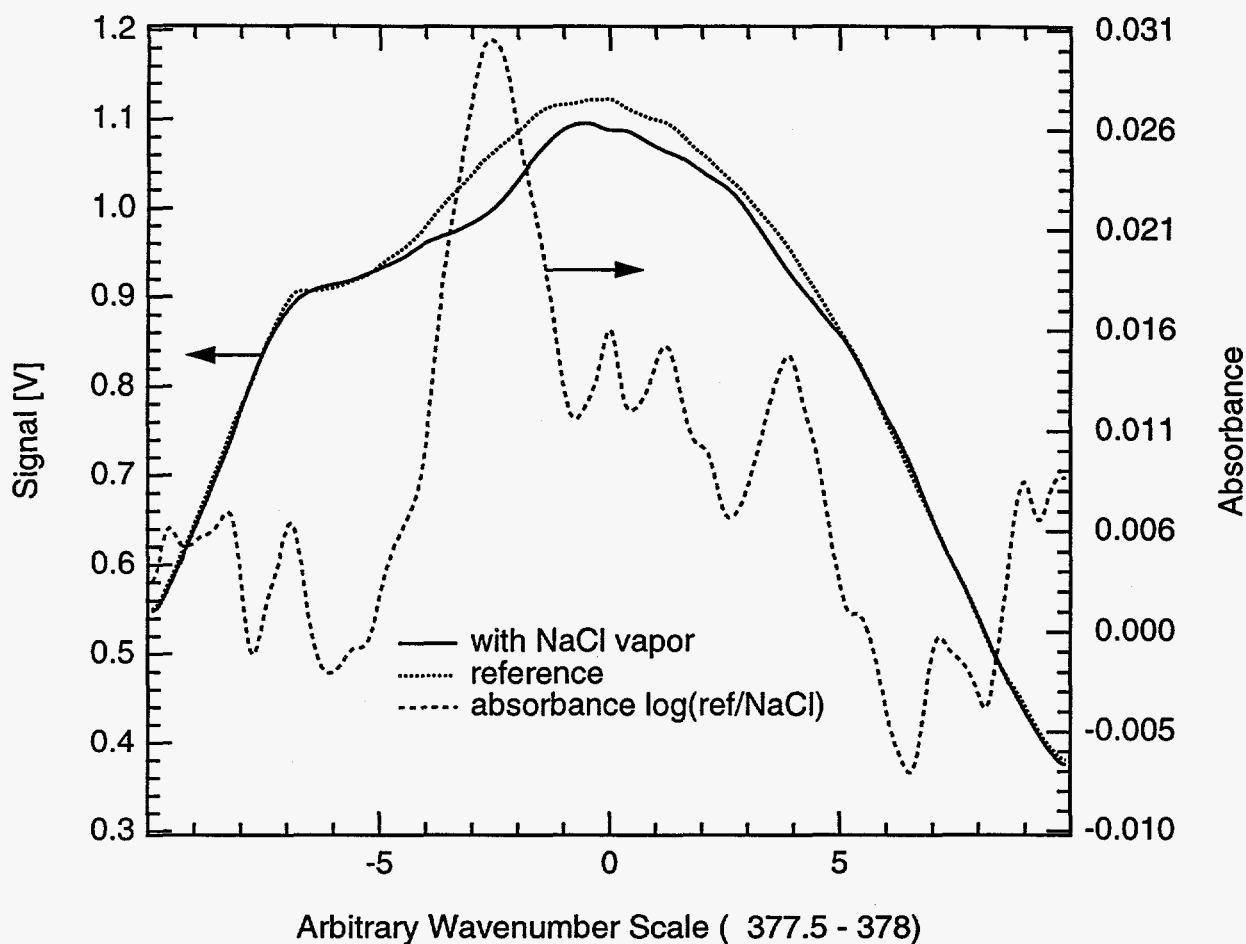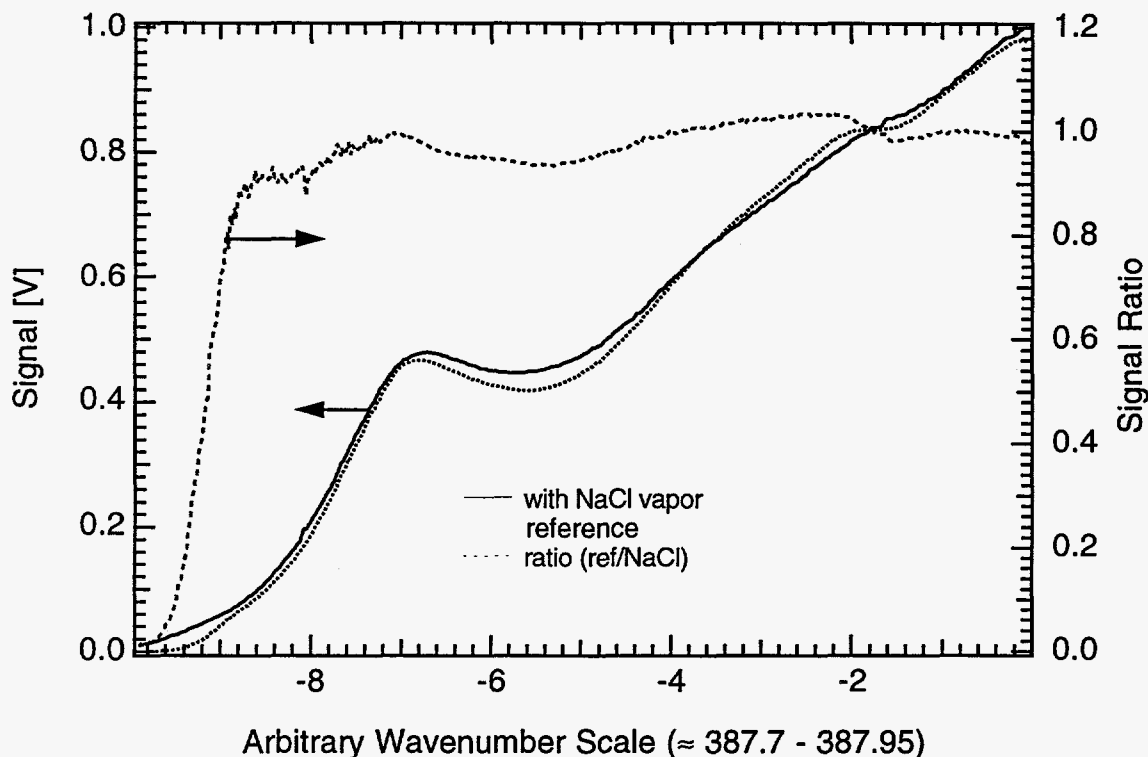

Figure 2.7   Reference and signal beams for the portion of the NaCl spectrum between approximately 387.7 and 387.95 wavenumbers.

All of the preceding data were collected at a diode temperature of 10 K. At higher diode temperatures, the laser has lower threshold currents, but lases at higher frequencies. At a diode temperature to 15 K the experiment was repeated in an attempt to detect the NaCl bandhead. The results are illustrated in Fig. 2.8. The data are indistinguishable indicating that the reference and probe beams are identical, within experimental error, over the entire region scanned. This indicates that the bandhead was not detected, although it could not have been missed by more than about 0.1 cm^{-1}.

Although the data of Fig. 2.8 are disappointing in the sense that the laser could not tune into the range of the bandhead, the data, nonetheless, make several contributions to the project. Because we are above the bandhead, we are reasonably confident that there are no other gas-phase species (e.g., CO_2 or H_2O) absorbing in this region. Therefore, the data provide a good indication of the noise resulting from our analysis — the noise is generally less than 2-3 % of the signal.
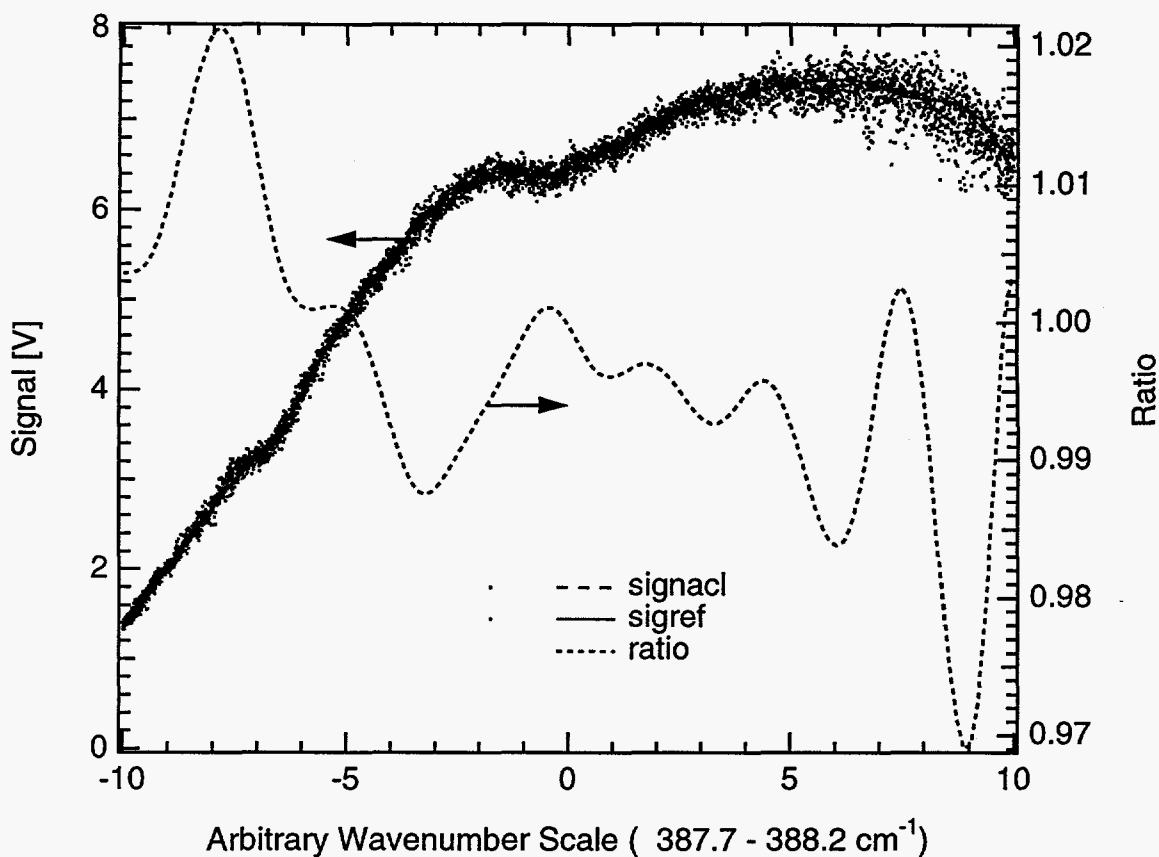
Figure 2.8   Results from scans slightly above the bandhead region of NaCl. Under these
experimental conditions, the laser could not tune to low enough frequencies to
detect the bandhead. The data permit good estimates of signal-to-noise ratios
and the affect of modulation of the laser current on the noise.

Future Work

The effect of modulating the current in the diode on the stability and accuracy of the laser has long
been a concern. The laser current increases linearly with increasing abscissa value in these figures.
The data in Fig. 2.8 reinforce the concern that switching the current on and off at 1 kHz disrupts
the stability of the laser since the noise clearly increases with increasing laser current, even when
total signal intensity is relatively constant. The accuracy of the laser is presumed to be similarly
affected, resulting in modestly, or perhaps strongly, chirped spectra (spectra consistent
wavenumber inaccuracies). We shall attempt to resolve this problem by mechanically chopping the
beam. An appropriate beam chopper that can modulate the beam at frequencies as high as 4 kHz
has been acquired for this purpose. There are advantages to modulating the beam at much higher
frequencies, but the all mechanical beam choppers we have been able to identify are limited to
around 4 kHz.

Data that we have obtained very recently indicate that we can detect the bandhead by further adjustment of temperature and current to the diode. The bandhead is the most forgiving feature of the spectrum to work with for quantitative measurement, but it is not absolutely necessary to detect it to make this a quantitative experiment. Future experiments will focus initially on improving signal-to-noise ratios, quantifying wavenumbers, and optimizing signals from the detector.

Reference gases and an etalon will be used to quantify the wavenumbers of the lasers. An etalon is currently available, but reference gases are that are active in this region are more difficult to indentify. NaCl itself will perhaps be our best reference, but will have to be analyzed at much lower pressures (20 Torr) to provide the resolution needed to serve as a calibration source. This will require completion of the furnace test cell with gas-tight, water-cooled windows.

FTIR Emission Spectroscopy

Development of FTIR emission spectroscopy continued this quarter with comparative analyses of coal ash deposits from eastern coals under conditions representing low-NO_x burner firing and traditional burner firing. The focus of this investigation is whether the FTIR spectrometer can be used to detect differences in the oxidation state of iron, the primary difference in deposits from high-rank coals fired with and without low-NO_x burners. This issue is of direct relevance to contractors involved in the Combustion 2000 program, and a complete discussion of the results is presented under Subtask 2.5. In summary, there was a consistent spectral difference noted in the deposits, and the difference corresponds with observed differences in deposit properties. These results, which emphasize application of the technique, were presented at the 1994 International Joint Power Generation Conference, which several of the Combustion 2000 contractors and subcontractors attended.

Development of the FTIR technique continues with emphasis on improving the data analysis and on improving our techniques for predicting the spectral features of particulate layers; the latter are related to the discussion below (see Subtask 2.3) of analysis of deposit reflectance properties. These improvements will be discussed in future quarterly reports.

Subtask 2.2   Experimental Determination of Transport, Thermal, and Structural Properties of Ash Deposits

Work continued this quarter on developing MFC diagnostics capable of *in situ*, time-resolved measurements of deposit thickness, surface temperature, mass, thermal conductivity, spectral emissivity, and porosity. Spectral emissivity measurements are accomplished by using the FTIR emission diagnostic being developed under Subtask 2.1. The remaining diagnostics are less involved and are being developed as a group under this subtask. Recent work has focused on measuring deposit thickness. The laser-based ranging device is functioning, but with less resolution and at slower data rates than we had anticipated. The instrument should be capable of resolving ± 8 μm, but our experience with stationary, room-temperature, shot-to-shot variations is that we observe $\approx \pm 180$ μm standard deviations, without filtering and averaging, and ± 30 μm standard deviations with filtering. We also are only capable of transferring measurements at 5 Hz, much slower than should be achievable based on the internal electronics. The computer-controlled

precision bearing and associated hardware used to scan the instrument along the length of a deposition probe appears to be functioning flawlessly.

An early design of a dynamic weighing diagnostic has been temporarily shelved while we investigate an improved design. The new design offers both higher resolution ($\pm$ 15 mg) and easier operation. The original design involved a load cell on the end of a cantilevered probe. While it appears that this design will work, it is relatively sensitive to vibration and requires the spatially resolved deposit thickness to determine a deposit mass. The new design addresses both of these issues by determining total mass with greater precision than is available from load cells. It will be discussed more completely in future reports.

The remaining diagnostics are essentially completed. We have yet to demonstrate the simultaneous measurements that we plan to make using them all. We anticipate no problems meeting our milestone for this demonstration.

Subtask 2.3 Analysis of Deposit Properties

An algorithm for predicting the reflectivity and emissivity of particulate layers was completed this quarter. This algorithm is sensitive to multiple scattering, porosity, composition, and particle size. It is fundamentally based, although the multiple scattering component is not as rigorous as the remaining portion of the algorithm. The algorithm has been coded and debugged. We are currently seeking ways to validate it analytically. An example prediction is indicated in Fig. 2.9.

The predictions indicate the bidirectional reflectance as a function of angle of incidence of light on a surface composed of particles with two different optical constants characterized by the albedo factor. The square of the albedo factor is equal to one minus the volume single scattering albedo. High albedo factors represent absorbing particles whereas low albedo factors represent scattering particles.

The figure illustrates the primary sensitivity of reflectance to the optical properties of the particles, with lesser sensitivities to the porosity of the layer or the size of the particles. There is far less sensitivity to size *per se* except as size impacts scattering properties. The peak in reflectance occurs near the angle of incidence (60°) and is called an opposition effect. This effect is sensitive to porosity, but less sensitive to size directly. Small particles often form particulate layers that are highly porous, yielding a functional dependence on size that is stronger than the mathematical dependence.

Subtask 2.4 Chemical Reactions in Deposits

No work was scheduled or performed on this task for this quarter.

Subtask 2.5 Application to Combustion 2000 Program

Experiments on SiC corrosion by alkali were completed this quarter, although data analysis is still underway. Early indications are that SiC corrosion proceeds under conditions where no sulfate is observed on the surface. Formation of silica and silicates is clearly evident in the spectra collected

from SiC samples exposed to high-temperature in the MFC. There is no indication of sulfate formation. Further analysis of the data will be reported in furture quarterly reports.
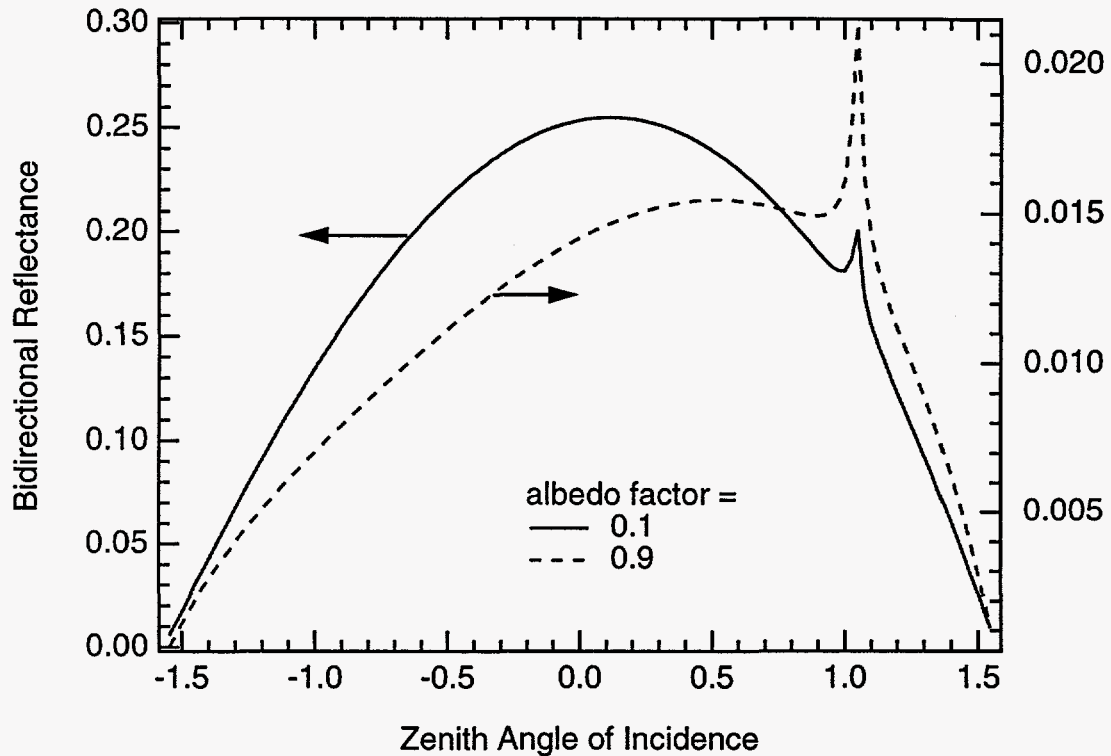
Figure 2.9   Illustration of the bidirectional reflectance as a function of angle of incident light for particles of significantly different scattering properties. The peak illustrated at about 1 radian is associated with an intense back scatter from granulated material known as the opposition effect.

An investigation of the effects of low-NO_x burners on ash deposits, focusing on the ability to detect such effects using the emission FTIR technique, was completed this quarter. The results from this investigation are reported below in the context of the issue. The focus of this investigation is whether the FTIR spectrometer can be used to detect differences in the oxidation state of iron, the primary difference in deposits from high-rank coals fired with and without low-NO_x burners. In summary, there was a consistent spectral difference noted in the deposits, and the difference corresponds with observed differences in deposit properties. These results were presented at the 1994 International Joint Power Generation Conference in a session attended by several of the Combustion 2000 contractors and subcontractors.

Effects of Low-NO$_x$ Burners on Ash Deposits

Summary

Increased rates of deposition and changes in deposit properties associated with the use of low-NO$_x$ burners are related to a combination of particle aerodynamics, combustion rates, and deposit chemistry. Under otherwise similar conditions, the principal cause of increased ash management problems in the furnaces with low NO$_x$ burners is related to the oxidation state of the iron. Ferrous iron (Fe^{+2}) can form unmanagable slag deposits at temperatures hundreds of degrees lower than ferric iron (Fe^{+3}). The former is present in more abundance when low-NO$_x$ burners or fuel/air staging are used. Methods of approach to describing ash deposit properties are presented and used to analyze conditions under which low-NO$_x$ burners will and will not lead to increased ash management problems. The potential impact of fuel properties and boiler operating conditions on ash deposit properties are also discussed. Illustrations from laboratory and field data are included.

Introduction

Empirical indices of ash deposition behavior have been developed and used by both operators and designers of coal combustors for several decades [Winegartner, 1974]. While the success of the current power generation industry attests to the usefulness of these indices, most people who have dealt with coal selection or boiler design recognize their limitations. In the past, many boilers were operated with a single fuel for most of their lifetimes, allowing experience to compensate for a lack of detailed knowledge about ash deposit formation mechanisms and their dependence on fuel type, operating conditions, and boiler design. Even so, most experts regarded ash deposition as the most significant factor controlling boiler operation and design [Raask, 1985]. The past practices of long-term commitments from single sources of fuel have largely disappeared. Responses to the Clean Air Act Amendments [1989], development of new utilization technologies, and expanded coal markets have all contributed to a more diverse set of ash-related problems in boilers. In many cases, these changes have worsened the ash deposition problems because of increased exposure to lower-rank fuels, high temperatures, or reducing conditions. The problem of ash deposition that many already viewed as the most daunting in the coal industry has, in many cases, become worse.

These changes challenge the capability of traditional coal indices to adequately anticipate problems in boilers. A significant amount of research has been performed in an attempt to reconcile observed behavior with fuel and boiler properties on a more scientific basis [Abbott, et al., 1993; Baxter, et al., 1991; Baxter and DeSollar, 1991; Beér, et al., 1990; Srinivasachar, et al., 1992; Zygarlicke, et al., 1992]. This paper presents a framework in which practical aspects of ash deposition can be discussed in terms that are scientifically sound and are common to engineers in both the power plant and research labs and applies it to the specific issues related to the use of low-NO$_x$ burners.

Ash Constraints on Boiler Operation

Formation of ash deposits in combustors depends on fuel properties, boiler design, and boiler operating conditions [Baxter, 1993a; Benson, et al., 1993]. Figure 2.10 illustrates some of the relationships among these factors. Deposit temperature and composition are both regarded as

independent variables in this figure. At a given deposit composition, temperature increases generally lead to increasingly tenacious and strong deposits. The line labeled Tenacity Threshold indicates the dividing line above which deposits cannot be removed from combustor walls by means available to the operator (soot or wall blowing, etc.). For example, as deposit temperature increases, components of the deposit begin to sinter and, consequently, the deposit develops strength and density. At some point, the deposit can no longer be removed from the surface on which it is formed. This point is indicated by the tenacity threshold line. As deposits change composition, the tenacity threshold also changes, as indicated in Fig. 2.10. The specific shape of the line depends on deposit thermodynamics and chemistry, and will be discussed later. For ash deposits to remain manageable, the deposits must be maintained below the tenacity threshold line.

Combustors are also subject to other constraints during operation. The principal constraint is that of meeting the steam generation load. Ash deposition problems could be avoided if temperatures were dramatically reduced, for example, by reducing, firing rate. However, efficient power generation requires that the heat transfer surface, and hence the deposit temperature, be maintained above some minimum value that is indicated in the figure as a Load Constraint. Successful operation of the boiler requires operating in regions that are both below the tenacity threshold line and above the load constraint. This region is labeled Operating Window in Figure 2.10.

This simplified view of ash management during boiler operation captures most of the first-order considerations. Recent advances in technology enable much more careful characterization of the tenacity threshold, relationships between deposit temperature and gas and steam temperatures, and relationships between deposit composition and fuel composition, boiler design, and boiler operating conditions. Boiler design influences both the deposit composition and the deposit temperature for any given fuel at a specified location in the boiler. However, boiler design cannot be changed rapidly or easily. For this reason, it is not considered a tool at the operators disposal to manage the ash deposition in the boiler. (It is the principal tool at the boiler designers disposal to manage ash deposition). This discussion focuses on fuel composition as it relates to deposit composition and boiler operating conditions and the relationship to deposit temperature, structure, and composition.

The representation illustrated in Fig. 2.10 is oversimplified in several respects. First, deposit composition cannot adequately be represented as a single parameter, as is suggested in Fig. 2.10. At least eight elements contribute significantly to overall deposit composition in coal-fired boilers (O, Si, Al, Fe, Ca, Na, K, and S) with several others playing a minor role (Ti, Mg, Cl, P, and C). Furthermore, these elements may be present in various chemical forms, with silicates, oxides, and sulfates the most common. Also, the morphology of the deposit influences its removability. A complete description of ash management requires more than a single parameter to characterize deposit composition, and therefore more sophisticated descriptions are being developed. The single-parameter-approach is used here primarily for illustration of what is inherently a multi-dimensional problem.

A second limitation of this approach to ash management is the specification of the tenacity threshold. Fundamentally, this threshold depends on the details of deposit structure — in particular the interface of the heat transfer surface and the deposit. The threshold varies with time, even in combustors operating under steady conditions, as chemical reactions drive deposits nearer

to their equilibrium compositions and as the deposit structure matures. Reactions between gas-phase species, such as alkali-containing vapors, and deposits also alter compositions. In some
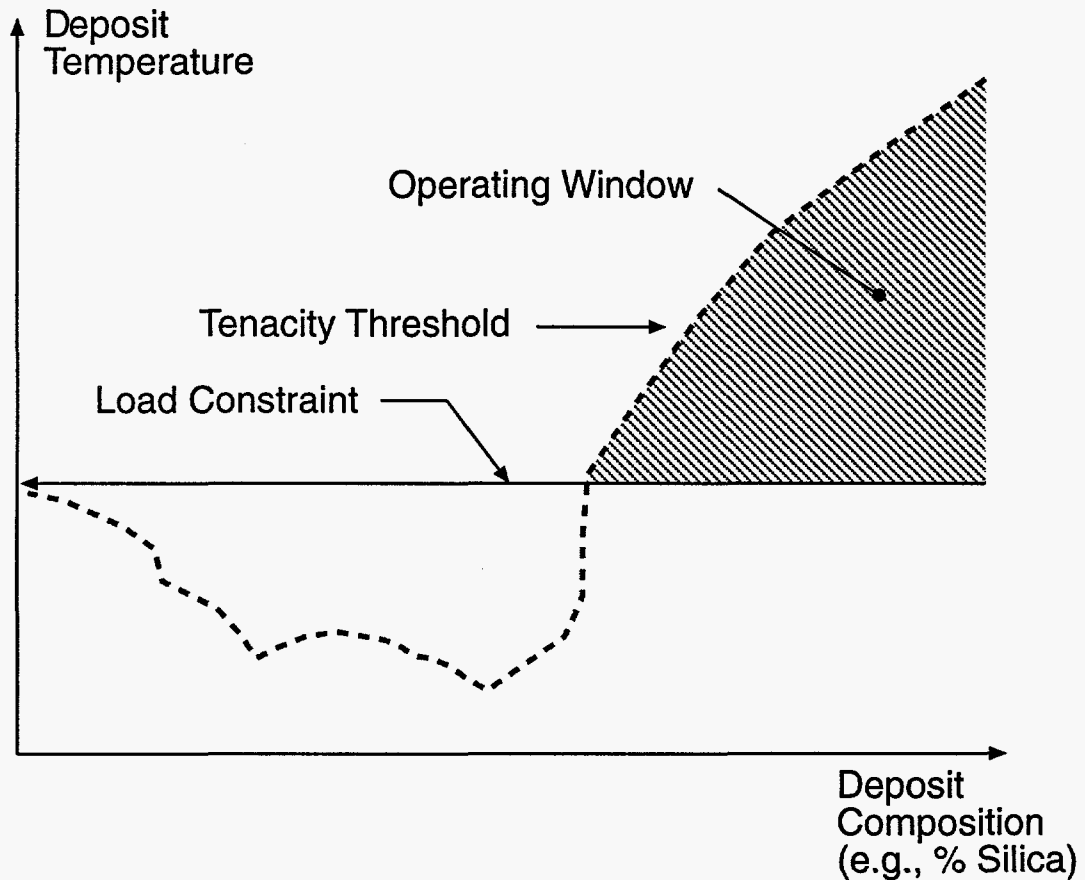
Figure 2.10 Schematic illustration of parameters that control successful operation of a boiler from the standpoint of ash management.

circumstances, deposit tenacity is strongly affected by the attraction of small particles to the surface rather than physical bonding. Finally, a tenacity threshold clearly depends on the location and efficiency of soot blowers and other boiler-specific considerations. All of these factors are difficult to incorporate in a single line such as is represented in Fig. 2.10. The approach here is to incorporate the most significant and common features of deposits that render them tenacious. These factors include (1) the formation of molten phases, and (2) the formation of sulfates or other possibly non-molten materials in intimate contact with the surface.

A third consideration is that ash deposits are not necessarily at chemical equilibrium with their environment. It takes time for condensed-phase reactions to occur and for materials to reach

equilibrium. While these time scales are very long compared to gas-phase reactions, they are typically comparable to controlling time scales for ash deposition. For example, between two soot blowing cycles (typically 8 hours minimum), high-temperature ash deposits can react significantly. Many reactions occur on time scales comparable to the residence time of fly ash [Srinivasachar, et al., 1990a; Srinivasachar, et al., 1990b]. While nonequilibrium considerations may expand the operating window slightly larger than is implied in Fig. 2.10, equilibrium properties represent a good point of departure for many applications.

This approach can be used to describe most of the features of ash deposits observed in several field tests and in pilot and laboratory tests in practically useful ways. The remainder of this report focuses on how to derive quantitatively the parameters indicated in the figure. The discussion briefly describes two examples.

Tenacity Threshold

The underlying concept in establishing the tenacity threshold is illustrated in Fig. 2.11. The feature of a deposit that makes it difficult to separate from a surface is the contacting efficiency and strength at the surface-deposit interface. On the left, a typical particle in a granular deposit is illustrated. The particle is rigid and is in intimate contact with the surface in only a small area. By comparison, the particle on the right is molten. The area of contact for the particle on the right is increased greatly compared to the particle on the left. This increase in contacting area is a primary mechanism whereby deposits develop tenacity. The change in contacting efficiency becomes even more pronounced if the surface and particle are have similar composition such that the particle wets the surface. Such may be the case for many iron-containing molten fly ash particles.

The fraction of the surface that is intimate contact with the deposit is defined as the contacting efficiency. Figure 2.12 illustrates how the relative volumes of molten material to particulate material (V_m/V_p) influences this contacting efficiency [Baxter and Dora, 1992]. The relative volume is the sum

of the volumes deposited by condensation or chemical reaction plus the fraction of particulate that is molten or was molten when it deposited on the surface (V_m) divided by the volume of ash deposited by inertial impaction or thermophoresis that is not molten (V_p). The details of these deposit formation mechanisms have been discussed elsewhere [Baxter and DeSollar, 1993]. Deposits with contacting efficiencies above approximately 0.10 are difficult to remove by traditional means. Typical deposits have particle volume fractions (ϕ) of about 0.3, ranging from 0.1 to 0.5. Under these conditions, no more than 5 to 10 percent of the deposit volume can be condensate or molten if the deposit is to be manageable (maintain a contacting efficiency of less than ten percent).

Effect of Low-NO$_x$ Burners on Ash Deposits

The formation of molten fractions of the deposit can be predicted by a combination of thermodynamic and chemical kinetic arguments. An illustration for interactions of sodium and silicon (components of most low-rank, US coals) is indicated in Figure 2.13.
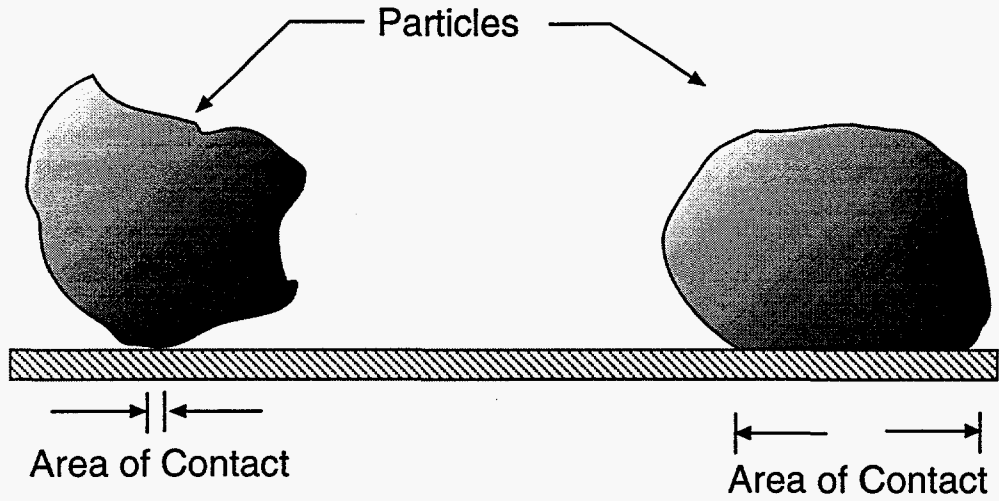
Figure 2.11   Illustration of the effect of molten particles on deposit contacting efficiency. Condensation has a similar effect.
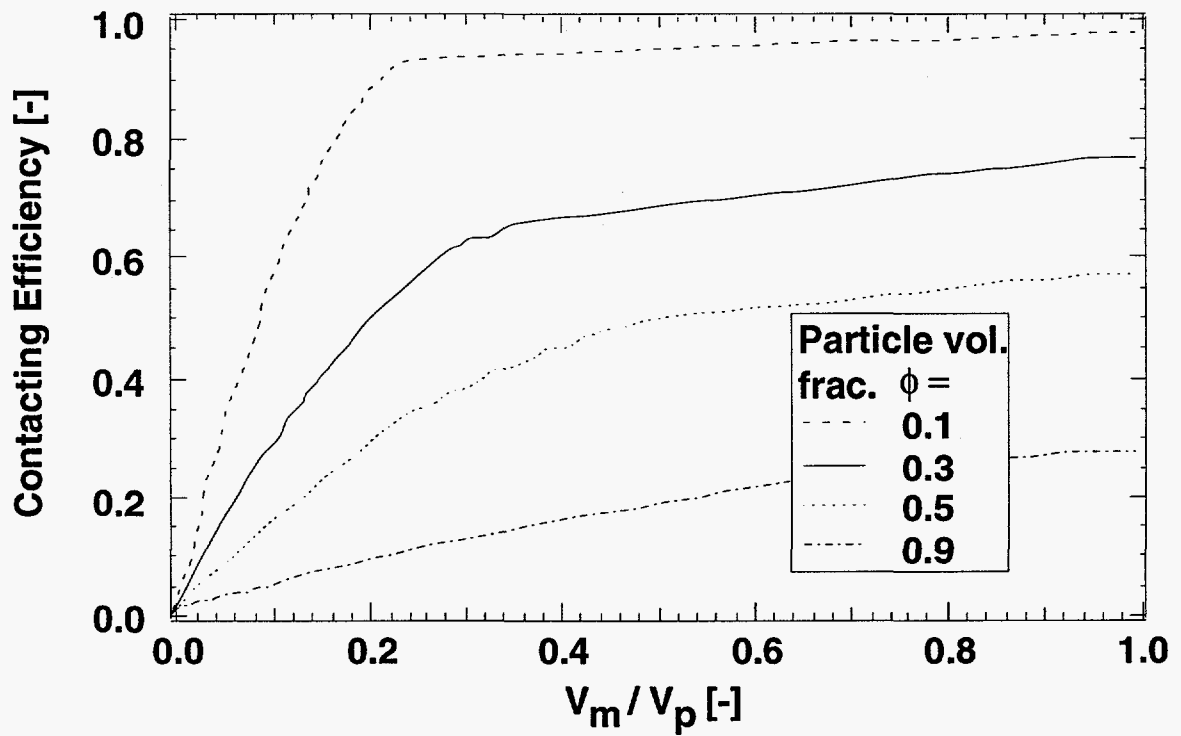

Figure 2.12   Quantitative dependence of contacting efficiency on relative proportions of molten on condensate volume to particulate volume.
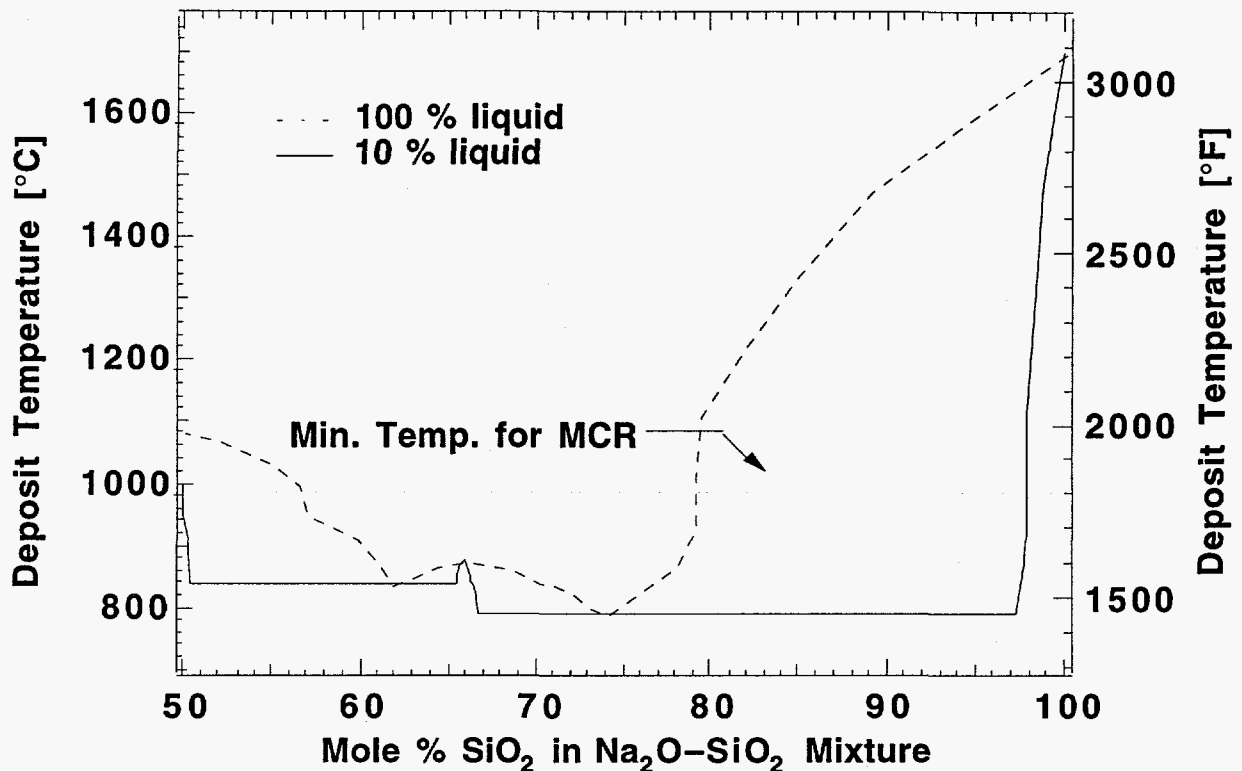
Figure 2.13   Melting behavior of a silica:sodium system commonly found in deposits
generated during low-rank coal combustion.

The figure indicates the temperatures at which 10 and 100 percent of this mixture of oxides
becomes liquid as a function of mixture (deposit) composition. As is indicated, if the deposit
contains greater than 3 mole % sodium oxide, the maximum deposit temperature that can be
allowed before forming more than 10 percent liquid is about 785 °C (1450 °F). The entire deposit
becomes molten at temperatures of around 1600 °C (3000 °F). Deposits in most practical systems
have more complex chemistry than can be easily illustrated in such a diagram, the addition of other
components changes the results significantly. For example, small amounts of calcium can lower
the melting temperatures illustrated in Fig. 2.13 even further, where as addition of aluminum
typically increases the melting temperature. Both aluminum and calcium are important constituents
of low rank coals.

Despite the complexity of more realistic mulicomponent systems, the concepts illustrated in
Fig. 2.13 are useful. Furnace exit gas temperatures in commercial coal-fired boilers range from
1800-2100 °F. Surface temperatures at the leading edge of deposits will rarely be lower than
1800 °F in such cases. This is indicated as the lower limit for operating at the maximum
continuous rating (MCR) in Fig. 2.13. The region above this minimum temperature and below the
10% liquid line represents the operating window for the boiler. This region is seen to be very
small for the case of deposits composed entirely of silica and sodium oxides. It is larger for most

2-23

coal systems that contain significant aluminum. The lowest melting point in the silica-alumina system, for example, is at 1584 °C (2883 °F).

One primary effect of low-NO_x burners with most eastern coals is to delay the oxidation of iron. The fuel-rich region generated by low-NO_x burners that is primarily responsible for the reduction in NO_x is also responsible for a decreased overall rate of oxidation of the particle. The most common form of iron in eastern coal is pyrite. The decomposition of pyrite (FeS_2) during combustion proceeds through a thermal decomposition to pyrrhotite (approximately Fe_7S_8), followed by oxidation to either hematite (Fe_2O_3) or magnetite (FeO), depending on local conditions [Baxter and Mitchell, 1992; Srinivasachar, et al., 1990a]. Pyrrhotite melts under many conditions relevant to boiler operation. The oxidation state of iron also plays a significant role in the formation of molten silicates. Mildly oxidized iron (Fe^{2+}) significantly decreases the melting point of silicates compared to more thoroughly oxidized iron (Fe^{3+}). This is illustrated in Fig. 2.14, where the temperature at which two mixtures of iron and silicon oxides melt is illustrated as a function of the iron content. Relatively modest amounts of FeO (Fe/(Fe+Si) $\approx$ 0.07) reduce the 10% melting point of the mixture significantly (<1200 °C), whereas the reduction in melting temperature for the mixture of FeO and Fe_2O_3 is less dramatic ($\approx$1450 °C) and occurs at higher iron concentrations (Fe/(Fe+Si) $\approx$ 0.20).

The lines in Fig. 2.14 correspond approximately to a tenacity threshold above which a boiler can no longer be operated without degradation of either equipment or power. In this case, the deposits are composed entirely of silica and iron oxides. In this simple illustration, switching to low-NO_x burners is comparable to changing the tenacity threshold from the solid line to the dashed line. If the load constraint is, for example, 1350 °C, such a switch clearly has the potential to significantly increase ash management problems over most of the range of deposit composition, i.e., the tenacity threshold is at a lower temperature than the load constraint over most of the range of deposit compositions.

Practical ash deposits exhibit more complex chemistry than is illustrated in Fig. 2.14, but the same qualitative trend is observed. One indication of this trend is the difference in the initial deformation temperature of ash deposits under reducing versus oxidizing conditions as a function of iron content. Figure 2.15 illustrates results of this standardized ash test for a range of coals studied in Sandia's Multifuel Combustor. These results show how the difference in the initial deformation temperatures under reducing and oxidizing conditions increases as the iron content increases.

The potential for increasing ash management problems by using low-NO_x burners is greatest for pyrite-containing (eastern) coals. There are second-order issues that may increase ash management problems for coals of all ranks. These include: (1) slower oxidation rates leading to larger particles that collide with walls with greater frequency; (2) locally reducing conditions enhancing the rate and amount of vaporized material; and (3) longer flames leading to greater potential of flame impingement on walls. These issues are usually of less importance if careful attention is paid to pulverizer performance, burner balancing, and fuel selection.

Traditional indices of ash deposition behavior often fail to describe ash deposition issues. For example, laboratory tests on over thirty commercially significant coals and about half as many

biomass fuels[1] have been performed in the Multifuel Combustor (Fig. 2.16), with many complementary studies performed at commercial sites. We contrast two of these results in Table 2.2, where the ash fusion temperatures (reducing conditions) are compared for one coal and one
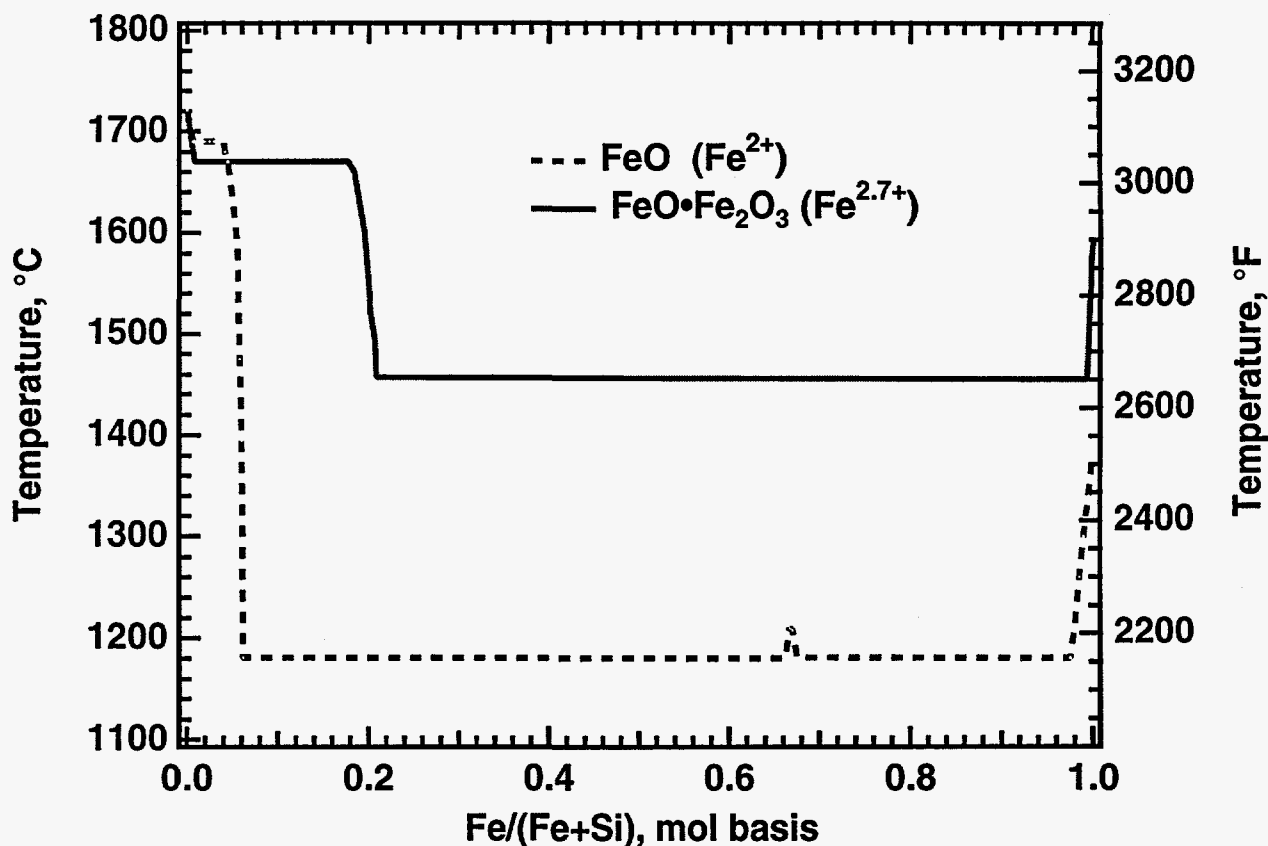
Figure 2.14   Effect of iron oxidation state on the temperature at which 10 % of a mixture of silica and iron oxides melts at equilibrium. The two lines indicate the different iron oxides mixed with silica. Results are based on published equilibrium phase diagrams [Levin, et al., 1964].

---

[1] The results described here for biomass fuels are derived from work conducted by Sandia in the Multifuel Combustor, in cooperation with the National Renewable Energy Laboratory, with support from the U.S. DOE Solar Thermal and Biomass Power Division. Comparison of the results obtained for coal and biomass fuels has been extremely useful in interpreting the data and deriving mechanistic information.
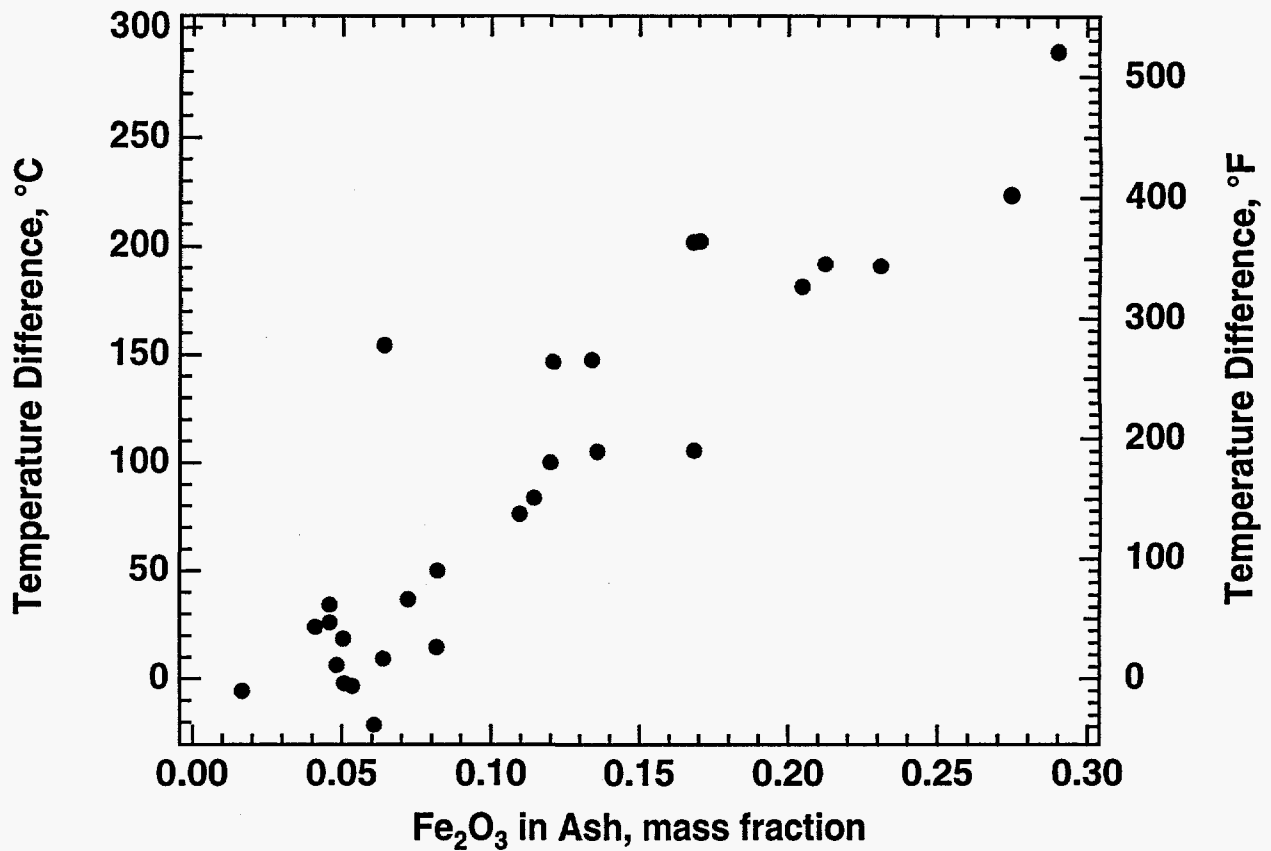
Figure 2.15 Difference in the initial deformation temperatures under oxidizing and reducing conditions for a suite of coals tested in Sandia's Multifuel Combustor.

biomass fuel (wheat straw). Both field and laboratory tests were performed for both of these fuels [Baxter and DeSollar, 1993; Baxter, et al., 1993a]. Note that the coal fusion temperatures are uniformly more than 100 °F lower. The straw heating value is about 70% that of this particular coal (as-fired basis). In the laboratory tests, the fuels were fired under the same conditions of gas temperature, oxygen concentration, burnout, and surface temperature. In the field, the straw was burned in a traveling-grate stoker-fired boiler with 50-60% excess air whereas the coal was burned in a tangentially fired pc boiler with 20% excess air. In both laboratory and field tests, the straw formed molten deposits at much lower temperatures than the coal. The wheat straw ash is composed of about 60% silica and 20% potassium, with about 3.5% calcium and less than 2% aluminum. The silicon is almost entirely in the form of free silica (as opposed to silicates) in fuel. The Hanna Basin ash comprises about 40% silica, 16% aluminum, 25% calcium. Silicon in the coal is primarily in the form of silicates.
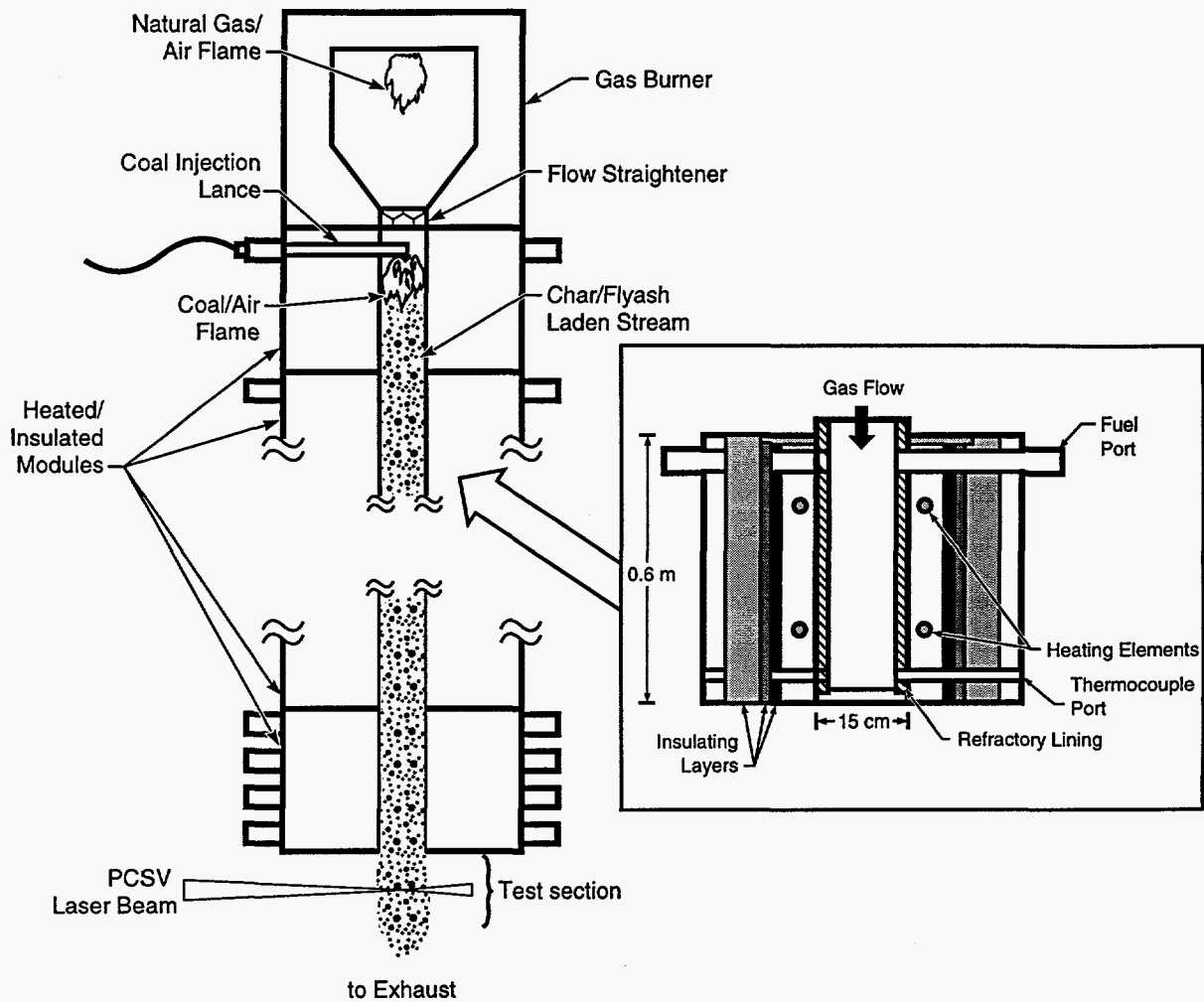
Figure 2.16   Schematic diagram of Sandia's MFC, where ash deposition tests under combustion conditions simulating commercial operation are conducted.

Note that the fuels in both laboratory and field tests behave opposite from what the fusion temperatures imply. The fuel with the highest fusion temperatures is the most prone to form molten slags. There are at least three potential reasons for the discrepancy: (1) the fusion temperature test is performed on ash from the fuel that may differ significantly in composition from the ash deposit in the boiler because of selective deposition; (2) the fusion temperature tests are performed quickly compared to the time available for ash deposits to react and form molten phases; and (3) the fusion temperature procedure uses ash samples that may be depleted in alkali during preparation (due to vaporization) and does not recreate the alkali-laden gas stream to which the actual deposits are exposed. Our observation was that as the wheat straw deposits matured on the surface of the laboratory system, potassium became increasingly incorporated in the silica matrix of the deposit. These results illustrate the need for improved conceptual approaches and

instrumentation when addressing ash deposition behavior. The conceptual approach discussed earlier and well-instrumented experimental facilities such as Sandia's MFC provide such resources.

Table 2.2

**Fusion temperatures and observed behaviors for
one coal and one biomass fuel.**

Fusion Temperature	Hanna Basin Coal		Wheat Straw	
(Reducing Condit).	°F	°C	°F	°C
Initial Deformation	2186	1196	2464	1351
Spherical	2245	1229	2466	1352
Hemispherical	2276	1246	2467	1353
Fluid	2338	1281	2474	1357
Observed Behavior	Dry, Granular, Easily Managed Deposit		Molten, Running Deposits Leading to Unscheduled Outage	

Deposit Management with Low-NO$_x$ Burners

Deposit management with low NO$_x$ burners is related to the mechanisms of deposit formation and operating conditions of the boiler. Deposit management techniques can be divided into coal preparation, burner operation, and boiler operation.

Coal Preparation

Small particles oxidize more rapidly and impact on surfaces less frequently than large particles. Since pyrite is a dense and strong material, it often is concentrated in the large size fractions of particles produced by commercial pulverizers. Controlling the top size of these particles either through classifier settings or rejecting pyrites from the mill is important for ash management for all burner systems. It is even more important when using low-NO$_x$ burners. By maintaining small particle size, particle impingement on surfaces can be minimized while maximizing rates of oxidation. Choosing coals with low iron contents, especially pyritic iron contents, is also helpful in minimizing ash deposit problems when using low-NO$_x$ burners.

Burner Operation

Flames from low-NO_x burners can extend further into the furnace than with previous burner designs. The potential for flame impingement on walls increases with these long, slender flames. Flame impingement is usually accompanied by significant ash deposition due to the high rates of impact of particles at high temperature and minimal extents of oxidation. The effect of minimal oxidation on the melting point of the deposit is illustrated in Figs. 2.14 and 2.15.

Laboratory and Field Experience

The onset of unmanageable ash deposits can be detected by several techniques. One property sensitive to the ratio between Fe^{+2} and Fe^{+3} is the deposit emissivity. Fig. 2.16 illustrates the ratio of emissivities observed for deposits generated from a Pittsburgh #8 coal at low and high extents of oxidation. The coal and deposit compositions are indicated in Table 2.3. The data are derived from *in situ*, real-time measurements of ash deposit emissivity in the particle-laden, turbulent flow environment of the MFC. The details of the optical and spectroscopic techniques are found elsewhere [Baxter, 1993b; Baxter, et al., 1993b; Richards, et al., 1994]. These data are in qualitative agreement with other studies of optical constant behavior [Goodwin, 1986], where the absorption coefficient of Fe^{+2}-containing slags was found to be below that of Fe^{+3}-containing slag in the visible and near-infrared region up to about 2 μm (5000 cm^{-1}), exceed that of Fe^{+3}-containing slag in the mid-infrared region of 2-5 μm (5000-2000 cm^{-1}), and be essentially the same in at wavelengths between 5 μm and 14 μm (2000 cm^{-1} to 714 cm^{-1}).

Table 2.3

Comparison of coal and deposit compositions for deposits generated in the MFC under identical conditions except for extent of oxidization.

Oxide	Coal	Partially Oxidized	Completely Oxidized
SiO_2	39.66	38.26	37.09
Al_2O_3	19.68	18.33	17.18
TiO_2	0.85	0.83	0.71
Fe_2O_3	27.79	34.73	35.52
CaO	4.54	2.91	4.09
MgO	0.85	0.67	0.66
K_2O	1.21	1.32	1.06
Na_2O	0.90	0.21	0.48
SO_3	4.18	2.23	2.87
P_2O_5	0.34	0.52	0.33

The deposit compositions are very nearly identical and similar to the coal composition, except for the amount of iron. Pyrite accounts for 92% of the total iron in this coal. The differences in the extent of oxidation of the deposits induce an observed emissivity difference (Fig. 2.16) and result in qualitatively observed differences in deposit tenacity and structure, with the less oxidized sample exhibiting greater tenacity and more sintered structure. Many traditional indices of ash deposition behavior (base to acid ratio and similar indices) do not distinguish between the oxidation state of the iron and would not be capable of predicting significant differences between the properties of the two deposits indicated in Table 2.3.
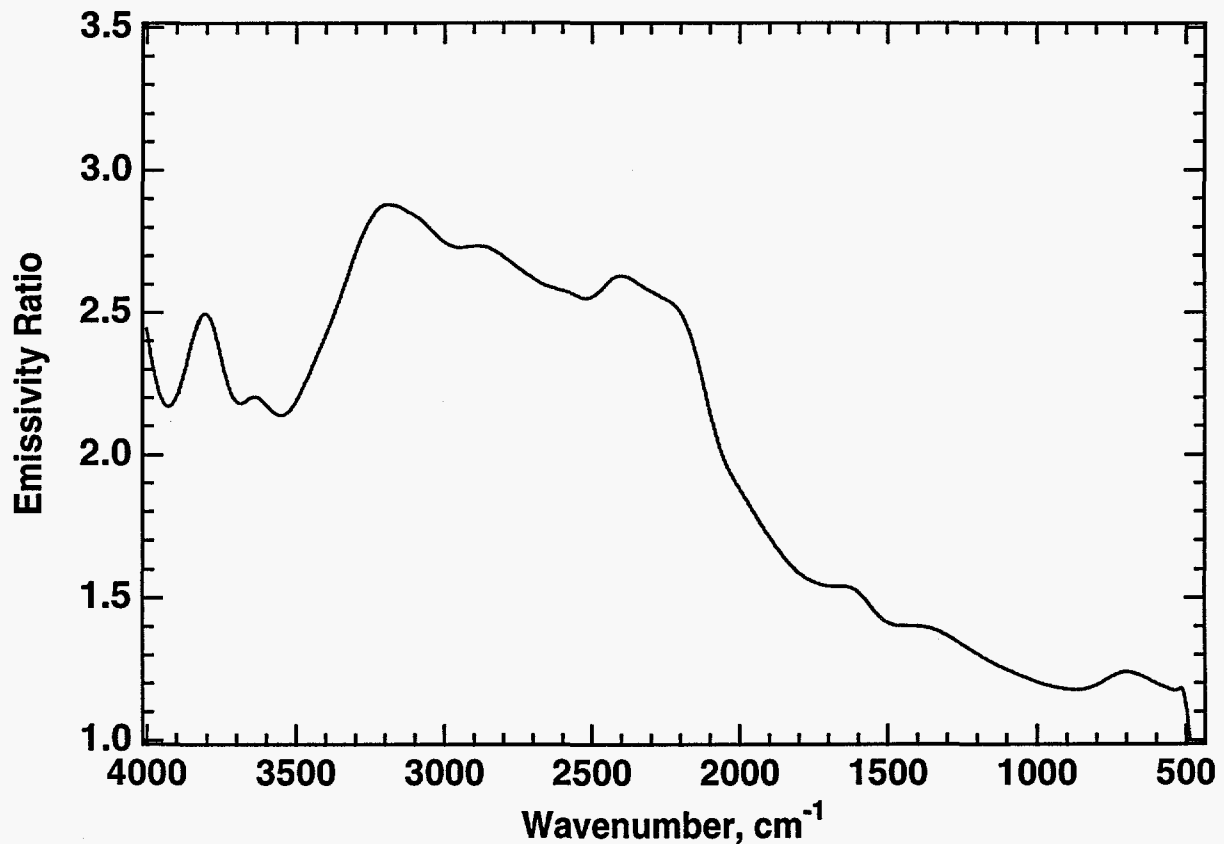
Figure 2.16 Ratio of spectral emissivities for ash deposits collected in the MFC under conditions of low and high extents of oxidation. Higher emissivities are associated with higher Fe^{+2} contents which, in turn, results from less extensive oxidation.

Similar differences are observed in field experiments. Reports from both low-NO_x burner use and fuel/air staging commonly indicate an increase in the amount and removal difficulty of the deposits [Couch, 1994; Makansi, 1993], with especially acute problems noted for boilers using coals with

high pyrite contents. The underlying reasons of these difficulties are believed to be associated with the decreased extent of iron oxidation and its affect of deposit properties, as outlined above.

Conclusions

The application of material equilibrium concepts and advanced technology are illustrated in addressing ash deposition problems. The constraints for long-term operation of a boiler can be viewed as a combination of local deposit temperature and composition. These, in turn, are controlled by fuel selection, boiler operating conditions, and boiler design. Thermodynamic equilibrium provides a useful point of departure for establishing the operating window. Equilibrium considerations combined with models of deposit tenacity can be used to predict deposit formation in conditions where traditional indices fail. Deposits are not in equilibrium initially, and the chemical reactions between ash constituents and gas-phase species that drive the composition toward equilibrium are shown to contribute significantly to critical regions of deposit strength, such as along heat transfer surfaces and between deposited particles. The combination of new diagnostics, sophisticated descriptions of materials, and careful experimentation is shown to improve understanding of deposit properties.

The use of low-NO_x burners potentially worsens ash deposit problems in boilers burning pyrite bearing coals since iron will not have sufficient time to oxidize completely. Ferric iron (Fe^{+2}), which is preferentially produced in reducing atmospheres, lowers the softening point of typical coal ashes by as much as 200-300 °C. The lower softening point increases deposit tenacity and strength, making deposits more difficult to manage. The problems become increasingly worse as iron content of the ash increases, temperatures increase, extent of exposure to reducing atmosphere increases, and particle size increases.

Methods of avoiding unmanageable ash deposits when using low-NO_x burners include: (1) monitoring of pulverizer performance to avoid large, pyrite bearing particles from entering the combustor; (2) avoiding flame impingement on walls to provide ample opportunity for iron to oxidize; (3) maintaining low gas and surface temperatures in regions near reducing environments; and (4) maintaining burner balance.

Subtask 2.6   Documentation

Publications, papers, and presentations during the last quarter are summarized below. In addition to these forms of communication, Sandia has been in frequent contact with several Combusiton 2000 contractors and subcontractors regarding the FTIR-spectroscopy-based analyses of SiC corrosion and forms of iron in deposits. In related work, Sandia is leading an effort by the ASME Research Committee on Corrosion and Deposits from Combustion Gases to quantify the potential economic benefits of increasing our ability to anticipate ash deposit properties.

PLANS FOR NEXT QUARTER

During the next quarter, work will continue with the tunable diode laser as outlined above. Alternate beam modulation techniques will be tested and further attempts to locate the NaCl bandhead will be pursued. Also, a sealed, high-temperature gas cell will be designed to allow

reference spectra to be obtained. Analyses of the first phase of the emission FTIR spectroscopy analyses of SiC surfaces in combustion environments will be completed. The theoretical description of the emissivity of particulate layers will also be expanded.

ACKNOWLEDGMENTS

Sandia Contributors

Gian Sclippa and Jimmy Ross (TAD Technical Services) are instrumental in operating and maintaining the MFC and associated equipment and in assisting in the design and construction of diagnostic and probe equipment as well as conducting TDL experiments. Peter Adams (Cornell) was instrumental in collecting and analyzing FTIR data from the SiC samples.

Industrial Contributors

Many of the chemical and physical analyses of solid samples of fly ash, deposits, and raw coal gathered during this investigation are performed by CONSOL Inc. with the assistance of Murray Abbott, Vince Conrad, and Diane Havekotte.

Academic Contributors

Prof. Peter Bernath (Universities of Waterloo and Arizona) and Postdoctoral Associate Dr. Ram Ram (Univ. of Arizona) are collaborating in the collection and analysis of inorganic vapor species compositions at high temperature. Mr. Alex Valle (HS student) worked on data acquisition and gas analysis systems, respectively.

PUBLICATIONS, PAPERS, AND PRESENTATIONS

The following presentations and papers based in whole or in part on PETC-supported work were completed in the last quarter.

Baxter, L.L., "The Effect of Low-NO$_X$ Firing on Formation of Ash Deposits," to be presented at the 1995 Engineering Foundation Conference on the Economic Aspects of Coal Utilization, Santa Barbara, CA, January 30 - February 3, 1995.

Baxter, L.L., "The effect of Low-NOx Firing on Fireside Performance," proceedings of the 1994 International Joint Power Generation Conference, Phoenix, AZ, October 3-5, 1995.

Baxter, L.L., R.E. Mitchell, T.H. Fletcher, and R.H. Hurt, "Nitrogen Release During Coal Combustion," submitted to *Energy & Fuels*, December 1995.

Baxter, L.L., Ash, to appear in the **Wiley Encyclopedia of Energy Technology**, 1995.

REFERENCES FOR TASK 2

(1989). "Federal Register: Part III; Air Contaminants" (Final Rule No. 29 CFR Part 1910).

Abbott, M. F., Douglas, R. E., Fink, C. E., Deluliis, N. J., and Baxter, L. L. (1993). "A Modeling Strategy for Correlating Coal Quality to Power Plant Performance and Power Costs". In *Engineering Foundation Conference on The Impact of Ash Deposition on Coal-Fired Plants*, . Solihull, England:

Baxter, L. L. (1993a). "Ash Deposition During Biomass and Coal Combustion: A Mechanistic Approach." *Biomass and Bioenergy, 4*(2), 85-102.

Baxter, L. L. (1993b). "In Situ, Real-Time Emission FTIR Spectroscopy as a Diagnostic for Ash Deposition During Coal Combustion". In *Engineering Foundation Conference on The Impact of Ash Deposition on Coal-Fired Plants*, . Solihull, England:

Baxter, L. L., Abbott, M. F., and Douglas, R. E. (1991). "Dependence of Elemental Ash Deposit Composition on Coal Ash Chemistry and Combustor Environment". In S. A. Benson (Ed.), *Engineering Foundation Conference on Inorganic Transformations and Ash Deposition During Combustion*, (pp. 679-698). Palm Coast, Florida: The American Society of Mechanical Engineers.

Baxter, L. L., and DeSollar, R. W. (1991). "Ash Deposition as a Function of Coal Type, Location in a Boiler, and Boiler Operating Conditions: Predictions Compared to Observations". In *International Conference on Environmental Control of Combustion Processes*, . Honolulu, HA:

Baxter, L. L., and DeSollar, R. W. (1993). "A Mechanistic Description of Ash Deposition During Pulverized Coal Combustion: Predictions Compared to Observations." *Fuel, 72*(10), 1411-1418.

Baxter, L. L., and Dora, L. (1992). "The Combustion Behavior of a Blend of Eastern and Western Coals: Comparisons Between a Blend and Its Individual Components." *ASME Paper No. 92-JPGC-FACT-14*.

Baxter, L. L., Miles, T. R., Miles, T. R., Jr., Jenkins, B. M., Richards, G. R., and Oden, L. L. (1993a). "Transformations and Deposition of Inorganic Material in Biomass Boilers". In M. G. Carvalho (Ed.), *Second International Conference on Combustion Technologies for a Clean Environment*, 1 (pp. Biomass II: 9-15). Lisbon, Portugal: Commission of European Communities.

Baxter, L. L., and Mitchell, R. E. (1992). "The Release of Iron During the Combustion of Illinois No. 6 Coal." *Combustion and Flame, 88*, 1-14.

Baxter, L. L., Richards, G. H., Ottesen, D. K., and Harb, J. N. (1993b). "*In Situ*, Real-time Characterization of Coal Ash Deposits Using Fourier Transform Infrared Emission Spectroscopy." *Energy & Fuels, 7*(6), 755-760.

Beér, J. M., Monroe, L. S., Barta, L. E., and Sarofim, A. F. (1990). "From Coal Mineral Matter Properties to Fly Ash Deposition Tendencies; a Modeling Approach". In *The Seventh International Pittsburgh Coal Conference*, . Pittsburgh, PA:

Benson, S. A., Jones, M. L., and Harb, J. N. (1993). "Ash Formation and Deposition." In L. D. Smoot (Eds.), *Fundamentals of Coal Combustion for Clean and Efficient Use* New York: Elsevier.

Couch, G. (1994). "Understanding slagging and fouling in pf combustion" No. IEACR/72). IEA Coal Research.

Goodwin, D. G. (1986) "Infrared Optical Constants of Coal Slags." Ph.D. Dissertation, Stanford University.

Levin, E. M., Robbins, C. R., and McMurdie, H. F. (1964). *Phase Diagrams for Ceramists*. Columbus, OH: American Ceramic Society.

Makansi, J. (1993). "Reducing NO_X emissions from today's power plants." *Power, 137*(5), 11-28.

Raask, E. (1985). *Mineral Impurities in Coal Combustion*. Washington: Hemisphere Publishing Corporation.

Richards, G. H., Harb, J. N., Baxter, L. L., Bhattacharya, S., Bupta, R. P., and Wall, T. F. (1994). "Radiative Heat Transfer in PC-Fired Boilers — Development of the Absorptive/Reflective Character of Initial Ash Deposits on Walls". In *Twenty-Fifth Symposium (International) on Combustion*, . Irvine, CA: The Combustion Institute.

Srinivasachar, S., Helble, J. J., and Boni, A. A. (1990a). "Mineral Behavior During Coal Combustion 1. Pyrite Transformations." *Progress in Energy and Combustion Science, 16*, 281-292.

Srinivasachar, S., Helble, J. J., Boni, A. A., Shah, N., Huffman, G. P., and Huggins, F. E. (1990b). "Mineral Behavior During Coal Combustion 2. Illite Transformations." *Progress in Energy and Combustion Science, 16*, 293-302.

Srinivasachar, S., Senior, C. L., Helble, J. J., and Moore, J. W. (1992). "A Fundamental Approach to the Prediction of Coal Ash Deposit Formation in Combustion Systems". In *The Twenty-Fourth Symposium (International) on Combustion*, (pp. in press). The University of Sydney, Australia: The Combustion Institute.

Winegartner, E. C. (1974). "Coal Fouling and Slagging" (Special Publication No. ASME.

Zygarlicke, C. J., Ramanathan, M., and Erickson, T. A. (1992). "Fly Ash Particle-Size Distribution and Composition: Experimental and Phenomenological Approach." In S. A. Benson (Eds.), *Inorganic Transformations and Ash Deposition During Combustion* (pp. 525-544). New York: American Society of Mechanical Engineers.

INITIAL DISTRIBUTION

Dr. Ralph Carabetta, Director
Office of Project Management
U.S. DOE/PETC
P.O. Box 10940
Pittsburgh, PA 15236-0940

Ms. Kay Downey
MS 58-M217
U.S. DOE/PETC
P.O. Box 10940
Pittsburgh, PA 15236-0940

Mr. James M. Ekmann
Director, Coal Combustion Division
U.S. DOE/PETC
P.O. Box 10940, MS 84-307
Pittsburgh, PA 15241

Dr. David Beecy, Director
Office of Advanced Research
Fossil Energy, FE-72
U.S. DOE/GTN
19901 Germantown Road
Germantown, MD 20585

Mr. G. Blair Martin, Associate Director
Office of Research and Development
Air Pollution and Prevention Control Division
US Environmental Protection Agency
MD-60
Research Triangle Park, NC 27711

Mr. Robert Wright
Office of Advanced Research
Fossil Energy, FE-72
U.S. DOE/GTN
19901 Germantown Road
Germantown, MD 20585

Mr. Philip M. Goldberg
Applied Science & Technology Division
U.S. DOE/PETC, 922-H
P.O. Box 10940
Pittsburgh, PA 15236-0940

Mr. James Hickerson
Power Division
U.S. DOE/PETC, 922-H
P.O. Box 10940
Pittsbrugh, PA 15236-0940

Dr. Gil McGurl, Director
Applied Science & Technology Division
Pittsburgh Energy Technology Center
Cochran Mill Road
Pittsburgh, PA 15236-0940

Dr. Larry Ruth, Director
Power Division
U.S. DOE/PETC
P.O. Box 10940
Pittsburgh, PA 15236-0940

Mr. James Jovanovich
PM-01, MS922-206
U.S. DOE/PETC, 922-H
P.O. Box 10940
Pittsburgh, PA 15236-0940

Dr. Everett Ramer
US DOE/PETC, 922-H
P.O. Box 10940
Cochran Mill Road
Pittsburgh, PA 15236-0940

Mr. A. E. Jacob Akanetuk
High Temperature Gasdynamics Lab
Bldg 520
Stanford University
Stanford, CA 94305

Professor Richard K. Chang
Department of Applied Physics
Yale University
P.O. Box 208284
New Haven, CT 06520-8284

Mr. Laurance L. Oden
Albany Research Facility, Bureau of Mines
U.S. Department of the Interior
Albany, OR 97321

Professor János Beér
Massachusetts Institute of Tech.
Department of Chemical Engineering
66-552
Cambridge, MA 02139

Prof. Peter Bernath
Chemistry Department
University of Waterloo
Waterloo, Ontario
Canada N2L 3G1

Professor Robert Essenhigh
Mechanical Engineering Department
Ohio State University
206 West 18th Avenue
Columbus, OH 43210

Professor Thomas H. Fletcher
Chemical Engineering Department
Brigham Young University
350 CB
Provo, UT 84602

Professor Robert Hurt
Division of Engineering, Box D
Brown University
Providence, RI 02912

Professor Bryan M. Jenkins
University of California, Davis
Biological and Ag. Eng. Dpt.
Davis, CA 95616-5294

Dr. Michael L. Jones
Energy and Mineral Research Center
University of North Dakota
Box 8213, University Station
Grand Forks, ND 58202
  Attn: Dr. Steve Benson

Professor John P. Longwell
Chemical Engineering Department
Massachusetts Institute of Technology
Room 66554
Cambridge, MA 02139

Professor Reginald E. Mitchell
High Temperature Gasdynamics Lab
Stanford University
Mechanical Engineering Department
Palo Alto, CA 94305

Professor Howard B. Palmer
Professor Emeritus of Energy Science
Fuel Science Program
The Pennsylvania State University
224 Academic Projects Building
University Park, PA 16802-2303

Professor Ronald Pugmire
Vice President for Research
University of Utah
210 Park Building
Salt Lake City, UT 84112

Professor Daniel E. Rosner
Director, High Temperature Chem Engr Lab
Yale University
P.O. Box 2159
New Haven, CT 06520-8167

Professor Adel Sarofim
Department of Chemical Engineering
Massachusetts Institute of Technology
66-466
Cambridge, MA 02139

Prof. Robert F. Sawyer
Professor of the Graduate School
72 Hesse Hall
University of California, Berkeley
Berkeley, CA 94720

Professor Philip Smith
Department of Chemical Engineering
University of Utah
2250 Merrill Engineering Bldg
Salt Lake City, UT 84112

Professor L. Douglas Smoot
Dept. of Chemical Engineering
Brigham Young University
265 L CTB
Provo, UT 84602

Professor Honghi Tran
Department of Chemical Engineering &
 Applied Chemistry
University of Toronto
200 College Street
Toronto, Canada M4S 1A4

Professor Terry Wall
Department of Chemical & Materials Engr.
The University of Newcastle
Newcastle, NSW 2308
Australia

Professor Jost Wendt
Department of Chemical Engineering
University of Arizona
Tuscon, AZ 85721

Prof. Judy Wornat
Mechanical & Aerospace Engineering Dept.
Princeton University
Room D329B, Engineering Quadrangle
Princeton, NJ 08544-5263

Dr. Seymour B. Alpert
P.O. Box 10412
Electric Power Research Institute
3412 Hillview Avenue
Palo Alto, CA 94308

Dr. Richard Bain, Manager
Biomass Power Program
National Renewable Energy Laboratory
1617 Cole Boulevard
Golden, CO 80401-3393

Mr. Richard W. Borio
Combustion Engineering Inc.
1000 Prospect Hill Road, P.O. Box 500
Windsor, CT 06095
  Attn: Mr. Michael Hargrove

Mr. Chester M. Bowling
Manager Tech. Support & Mrktng
ARCO Coal Company
555 Seventeenth St.
Denver, CO 80202

Mr. Richard W. DeSollar
Fuels Coordinator
Central Illinois Public Service Co.
607 East Adams Street
Springfield, Il 62701

Mr. Lawrence L. Dora
O&M Manager
NIPSCO/R. M. Schahfer Gen. Station
2723 E. 1500 N.
Wheatfield, IN 46392

Dr. Thomas H. Dunning, Jr., Director
Environmental Molecular Sciences Lab
Molecular Science Research Center
Pacific Northwest Laboratories
P.O. Box 999, MS K2-20
Richland, WA 99352

Dr. Woodrow Fiveland, Supervisor
Heat Transfer & Fluid Mechanics Section
Babcock & Wilcox
1562 Beeson St.
Alliance, OH 44601

Dr. Patrick F. Flynn, Vice President
Research & Technology
Cummins Engine Company
Mail Code 50181, Box 3005
Columbus, IN 47202-3005

Dr. J. Peter Gorog
Research and Development
Pulp, Paper and Packaging
Weyerhaeuser Company
WTC 2H22
Tacoma, WA 98477

Dr. Evan Hughes
Manager, Renewable Fuels
Electric Power Research Institute
3412 Hillview Avenue
P.O. Box 10412
Palo Alto, CA 94303

Mr. Peter Torslev Jensen
ELSAM
Fuel Department
DK-7000 Fredericia
Denmark

Dr. Flynt Kennedy, Vice President
Research & Development
Consolidation Coal Co.
4000 Brownsville Road
Library, PA 15129
  Attn: Dr. Anthony Fonseca

Dr. John Lytle
Mineral Engineering Laboratory
Illinois State Geological Survey
Oak and Gregory Sts.
Champaign, IL 61820

Mr. John H. (Jack) Matkin, Manager
Fuels & Processing Technology Group
Chevron Research & Technology
P.O. Box 1627
Richmond, CA 94802-0627

Dr. John S. Maulbetsch
Exploratory Research
Electric Power Research Institute
3412 Hillview Avenue
Palo Alto, CA 94303

Dr. Arun K. Mehta
P.O. Box 10412
Electric Power Research Institute
3412 Hillview Avenue
Palo Alto, CA 94308

Mr. Thomas R. Miles
Consulting Design Engineer
5475 SW Arrowwood Lane
Portland, OR 97225

Dr. Thomas Milne
National Renewable Energy Laboratory
1617 Cole Boulevard
Golden, CO 80401-3393

Dr. Ralph P. Overend
National Renewable Energy Lab
1617 Cole Boulevard
Golden, CO 80401-3393

Mr. John R. Rackley, Vice President
Research & Development
Babcock & Wilcox
1562 Beeson Street
Alliance, OH 44601

Mr. Eric H. Reichl
P.O. Box 472
Princeton, NJ 08542

Dr. Dan Seery
United Technologies Research Center
Combustion Sciences
Silver Lane, MS 30
East Hartford, CT 06108

Mr. Ian W. Smith, Manager
Coal Utilization Program, CSIRO
51 Delhi Road, P.O. Box 136
North Ryde, NSW, 2113
Australia

Mr. Jerry Sullivan, Project Director
PSI Energy
1000 East Main Street
Plainfield, IN 46168

Dr. David A. Tillman
Foster Wheeler Environmental Corporation
2525 Natomas Park Drive, Suite 250
Sacramento, CA 95833-2900

Mr. Stanley Vecci, Director
Energy Systems Lab/Research Dev Div
Babcock & Wilcox
1562 Beeson Street
Alliance, OH 44601
 Attn: Mr. John Berthold
       Mr. Thomas Morris
       Mr. Larry Rodgers
       Dr. Hamid Sarv
       Mr. James Warchol
       Mr. Ralph Bailey
       Mr. George Farthing

Mr. Craig G. Vogel
Manager, Technical Sales
Cyprus Coal Company
9100 East Mineral Circle
Englewood, CO 80112

Mr. Ben Ziesmer
Fuel Coordinator
Northern Indiana Public Services Co.
5265 Hohman Ave.
Hammond, IN 46320

MS0828	P. J. Hommert, 1503	
MS0701	R. W. Lynch, 6100	
MS0735	D. E. Arvizu, 6200	
Attn:	6211	G. A. Carlson
	6212	H. R. Stephens
	6203	A. P. Sylwester
MS0704	P. C. Klimas, 6201	
Attn:	6215	J. Chavez
	6215	K. S. Rawlinson
MS9001	T. O. Hunter, 8000	
Attn:	8100	M. E. John
	8200	L. A. West
	8400	R. C. Wayne
	8800	L. A. Hiles
MS9054	W. J. McLean, 8300	
Attn:	8345	C. M. Hartwig
	8351	L. A. Rahn
	8353	F. P. Tully
	8355	G. A. Fisk
	8362	R. W. Carling
	8366	R. W. Gallagher
MS9052	L. L. Baxter, 8361	
MS9052	S. G. Buckley, 8361	
MS9052	D. R. Hardesty, 8361 (15)	
MS9052	S. P. Huey, 8361	
MS9052	M. M. Lunden, 8361	
MS9052	S. F. Rice, 8361	
MS9052	J. R. Ross, 8361	
MS9052	G. Sclippa, 8361	

MS9052　C. Shaddix, 8361

MS9052　S. Sinquefield, 8361

MS9007　J. Swearengen, 8419

MS9401　M. T. Dyer, 8700
　Attn:　　8711　M. W. Perra
　　　　　 8712　M. I. Baskes
　　　　　 8712　B. Fuchs
　　　　　 8713　D. K. Ottesen
　　　　　 8713　J. C. F. Wang

MS9402　N. Y. C. Yang, 8714

MS9402　G. Thomas, 8715

MS9021　Technical Communications Department, 8815
　　　　　for OSTI (10)

MS9021　Technical Communications Department, 8815
　　　　　Technical Library, MS0899, 4414

MS0899　Technical Library, 4414 (4)

MS9018　Central Technical Files, 8950-2 (3)